Title

Highly-multiplexed volumetric mapping with Raman dye imaging and tissue clearing

Journal

Nature Biotechnology, 40(3)

ISSN

1087-0156

Authors

Shi, Lixue
Wei, Mian
Miao, Yupeng
et al.

Publication Date

2022-03-01

DOI

10.1038/s41587-021-01041-z

Peer reviewed

nature biotechnology

ARTICLES

https://doi.org/10.1038/s41587-021-01041-z

Highly-multiplexed volumetric mapping with Raman dye imaging and tissue clearing

Lixue Shi[1,7], Mian Wei[1,7], Yupeng Miao[1], Naixin Qian[1], Lingyan Shi[1,5], Ruth A. Singer[2,6], Richard K. P. Benninger[3] and Wei Min[1,4] ✉

Mapping the localization of multiple proteins in their native three-dimensional (3D) context would be useful across many areas of biomedicine, but multiplexed fluorescence imaging has limited intrinsic multiplexing capability, and most methods for increasing multiplexity can only be applied to thin samples (<100 μm). Here, we harness the narrow spectrum of Raman spectroscopy and introduce Raman dye imaging and tissue clearing (RADIANT), an optical method that is capable of imaging multiple targets in thick samples in one shot. We expanded the range of suitable bioorthogonal Raman dyes and developed a tissue-clearing strategy for them (Raman 3D imaging of solvent-cleared organs (rDISCO)). We applied RADIANT to image up to 11 targets in millimeter-thick brain slices, extending the imaging depth 10- to 100-fold compared to prior multiplexed protein imaging methods. We showcased the utility of RADIANT in extracting systems information, including region-specific correlation networks and their topology in cerebellum development. RADIANT will facilitate the exploration of the intricate 3D protein interactions in complex systems.

Biological systems consist of a large number of interacting components in their native 3D environment. This theme recurs at nearly every length scale, ranging from protein networks to organelles within cells, various cell types within tissues and synergistic tissues within functional organs and reaching maximum complexity in the nervous system. Indeed, numerous highly diversified cell types exist and intermix in the central nervous system. For example, in the frontal cortex alone, a recent methylome study identified at least 16 neuronal subtypes in mice and 21 neuronal subtypes in humans[1]. Moreover, individual neurons can extend in many directions and project over long distances[2]. Hence, mapping multiple proteins over a large volume is critical in understanding complex biological systems.

Fluorescence microscopy is the prevalent technique for protein imaging. However, due to fast electronic dephasing, the fluorescence spectrum is too broad to spectrally resolve many targets at once, known as the 'color barrier' (Fig. 1). As a result, typically no more than five targets can be simultaneously imaged (or seven using specialized instrumentation and analysis[3,4]). To visualize a large number of targets at the same time, highly multiplexed protein-imaging techniques have been developed. However, these methods are mostly confined to relatively thin samples (Fig. 1). Mass spectrometry-based methods are inherently surface techniques[5,6]. Cyclic immunofluorescence performs multiple (often greater than ten) rounds of labeling, antibody stripping (or photobleaching) and restaining[7–10]. However, cyclic methods are extremely difficult to apply to thick tissues due to several inherent limitations. First, multiple rounds of 3D immunostaining could take an unpractically long time; 3–8 d are typically required for antibodies to penetrate into 1-mm-thick tissues (Supplementary Table 1), and, hence, ten rounds of staining and destaining will be prohibitively lengthy. Second, repeated tissue processing, especially volumetric antibody stripping and postclearing restaining, can cause accumulated antigen loss and fine structural damage[5]. CLARITY reported three cycles on 1-mm-thick tissue[11], but possibly with compromised structural and antigen integrity[12,13]. Third, 3D image co-registration and subsequent inference becomes much more difficult than the two-dimensional counterpart due to non-linear volumetric histological changes among different cycles[5]. Owing to these limitations, despite recent innovations on engineering tissues[13–15], cyclic immunofluorescence has only been demonstrated in a relatively superficial depth (~100 μm) with a limited number of cycles even in the best case scenario. Thus, in spite of its perceived importance, highly multiplexed protein imaging in large 3D volume remains uncharted.

Our premise is that the above difficulties can be overcome if one can use a one-shot optical method. To develop such technology, we harness advanced Raman microscopy. Owing to much narrower vibrational peaks (~10 cm^{-1}) than fluorescence (~500 cm^{-1}), Raman imaging can, in principle, break the fluorescence color barrier[16]. For example, Cy5, one of the most commonly used fluorescent dyes, shows a 50-nm (~700 cm^{-1}) full width at half maximum (FWHM) in the fluorescence spectrum, but the Raman signature of its double bond in the fingerprint region is only 12 cm^{-1} in width[16]. Thus Raman spectroscopy poses a fundamental advantage for multiplexing in one shot. However, its sensitivity is generally far from ideal for imaging specific proteins inside cells[17]. Recently, by combining electronic preresonance spectroscopy with stimulated Raman scattering (SRS) microscopy (that is, epr-SRS), the Raman cross sections of electronically coupled vibrational modes in light-absorbing dyes can be enhanced by 10^{13}-fold[16,18]. As a result of this drastic enhancement, we achieved nanomolar sensitivity of Raman-active dyes (such as commercial far-red fluorescent dyes and specially designed Manhattan Raman scattering (MARS) probes with conjugated triple bonds[19]) and demonstrated epr-SRS imaging of specific

[1]Department of Chemistry, Columbia University, New York, NY, USA. [2]Graduate Program in Cellular, Molecular and Biomedical Studies, Columbia University Medical Center, New York, NY, USA. [3]Department of Bioengineering, University of Colorado Anschutz Medical Campus, Aurora, CO, USA. [4]Kavli Institute for Brain Science, Columbia University, New York, NY, USA. [5]Present address: Department of Bioengineering, University of California San Diego, La Jolla, CA, USA. [6]Present address: Laboratory of Molecular Neuro-oncology, Rockefeller University, New York, NY, USA. [7]These authors contributed equally: Lixue Shi, Mian Wei. ✉e-mail: wm2256@columbia.edu

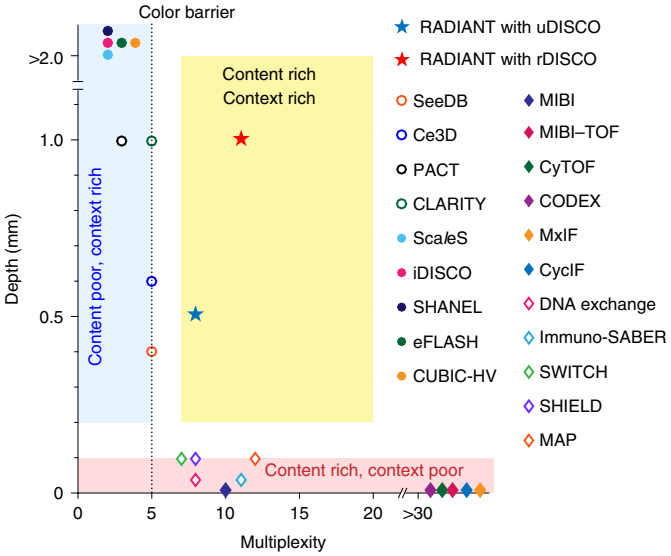

Fig. 1 | The limitations of existing protein-imaging methods toward highly multiplexed volumetric protein imaging. A summary including the details of the listed methods can be found in Supplementary Table 1; color barrier, typically no more than five colors can be detected simultaneously by fluorescence microscopy. A general trade-off between content (high multiplexity) and context (thick samples) restricts the use of existing protein-imaging methods toward highly multiplexed volumetric protein imaging. RADIANT breaks the content–context trade-off (yellow region); uDISCO, ultimate DISCO; SeeDB, see deep brain; Ce3D, clearing-enhanced 3D; PACT, passive clarity technique; CLARTY, clear lipid-exchanged acrylamide-hybridized rigid imaging/immunostaining/in situ hybridization-compatible tissue-hydrogel; Sca*l*eS, sorbitol-based sca*l*e; iDISCO, immunolabeling-enabled DISCO; SHANEL, small-micelle-mediated human organ efficient clearing and labeling; eFLASH, electrophoretically driven fast labeling using affinity sweeping in hydrogel; CUBIC-HV, CUBIC-HistoVIsion; MIBI, multiplexed ion beam imaging; TOF, time of flight; CyTOF, cytometry by time of flight; CODEX, codetection by indexing; MxIF, multiplex immunofluorescence; CycIF, cyclic immunofluorescence; immuno-SABER, immunostaining with signal amplification by exchange reaction; SWITCH, system-wide control of interaction time and kinetics of chemicals; SHIELD, stabilization to harsh conditions via intramolecular epoxide linkages to prevent degradation; MAP, magnified analysis of the proteome.

proteins inside cells[16]. Hence, the sensitivity issue of protein imaging by Raman microscopy is largely solved (Supplementary Note 1). However, as an optical technique, imaging depth of epr-SRS is still limited by the inevitable light scattering inside biological tissues. As a result, the epr-SRS imaging reported so far was performed only on thin tissue sections.

Thus we aim to generalize epr-SRS to large-scale volumetric imaging. Our inspiration comes from the recent success of tissue-clearing technology, a powerful strategy to gain deep optical access inside tissues by homogenizing refractive indices[20,21]. However, the coupling of epr-SRS with tissue clearing can be easily hampered by the high-concentration chemicals inside refractive index-matching solutions (RIMS), which could produce overwhelming Raman background, interfering with the desired signature of Raman-active dyes. To explore this unknown paradigm, we adopted a systematic strategy to optimize the coupling between epr-SRS microscopy and tissue clearing. We started by examining the spectral compatibility of Raman-active dyes with tissue-clearing protocols. The results suggested unsuitability of commercial dyes for this task and prompted us to develop new bioorthogonal vibrational probes. These new probes allowed for immuno-eprSRS imaging of various protein targets in diverse tissue types under different sample preparations. We then screened and compared common tissue-clearing methods for volumetric epr-SRS imaging, and the obtained insights led to our optimization of rDISCO as a Raman dye-tailored tissue-clearing method. With the synergistic developments along both probes and tissue clearing, we achieved one-shot multiplexed imaging of more than ten targets in millimeter-thick brain tissues, which extends the imaging depth of the current best volumetric cyclic immunofluorescence results by tenfold. We name this new method RADIANT, which has unique advantages for thick tissues in that antibody staining and imaging can be performed for all targets in one shot, thereby circumventing the abovementioned limitations with cyclic immunofluorescence techniques. We further demonstrated its utility in extracting systems information, including regional segmentation, spatial correlation, cellular composition, 3D distance and network topology, during cerebellum development.

Results

Compatibility study of Raman dyes with tissue clearing. As tissue clearing is almost exclusively developed for fluorescence microscopy, we need to first study whether Raman-active dyes can be imaged after tissue-clearing protocols. A potential pitfall, which is new for Raman microscopy but not for fluorescence, is the interfering Raman background from the high-concentration chemicals used in RIMS that are required by all tissue-clearing methods.

It is a common practice in the Raman field to use commercial Raman-active dyes for multiplexed detection in the fingerprint region (500–1,700 cm^{-1})[22]. To study their spectral compatibility with RIMS, we picked MitoTracker deep red and ATTO 740 as two model compounds[16] and used the RIMS from popular tissue-clearing methods, such as sorbitol-based sca*l*e (Sca*l*eS)[23], ultrafast optical clearing method (FOCM)[24], clearing-enhanced 3D (Ce3D)[25], 3D imaging of solvent-cleared organs (3DISCO)[26] and ultimate DISCO (uDISCO)[27], to represent the final imaging media. As expected, the fluorescence signals of MitoTracker were background free in all the RIMS used in the test (Extended Data Fig. 1a). However, the epr-SRS signals of both MitoTracker and ATTO 740 suffered from interfering Raman backgrounds in the fingerprint region originating from the RIMS with varying extent (Extended Data Fig. 1b,c). In particular, the backgrounds from RIMS in 3DISCO and uDISCO completely overwhelmed the signal from MitoTracker. Similarly, ATTO 740 signal was largely buried in the background from RIMS in Ce3D. The epr-SRS imaging results can be explained by the relative Raman spectral intensities acquired for RIMS in this fingerprint region (Extended Data Fig. 1d).

The above incompatibility of commercial Raman-active dyes with tissue clearing urges us to look for spectral features outside the fingerprint region. Epr-SRS imaging also works for specially engineered MARS dyes, which uniquely use π-conjugated triple bonds (hence, gain electronic enhancement in epr-SRS excitation) as the bioorthogonal Raman reporters in the cell-silent spectral region (1,800–2,800 cm^{-1})[16,19,28]. Because of the structural and spectral similarity of all MARS dyes, we picked a MARS dye as a model system to study the spectral compatibility with those RIMS. Remarkably, epr-SRS imaging of the MARS dye was free from background interference of all the tested RIMS, indicating that MARS dyes were spectrally orthogonal to all the solutions tested (Extended Data Fig. 1e). This desirable feature emerges because all clearing reagents are Raman transparent in the spectral range (2,000–2,400 cm^{-1}) of the reporter triple bonds (Extended Data Fig. 1f), indicating spectral compatibility of the entire MARS palette with all the common RIMS. We hence selected the bioorthogonal MARS dyes over conventional/commercial dyes as the imaging probes for RADIANT.

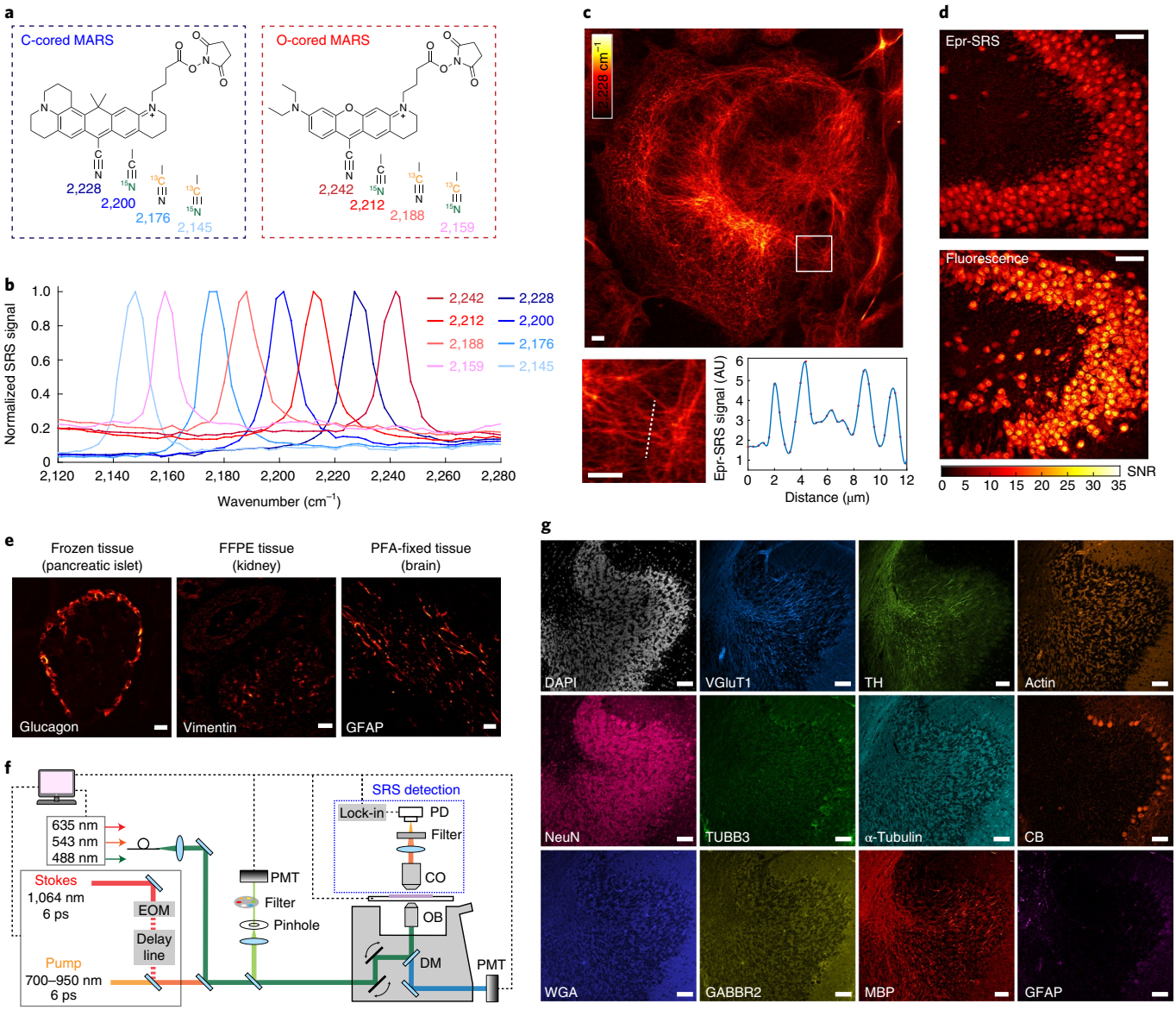

Fig. 2 | Selection and expansion of MARS palette for one-shot multiplexed protein imaging. a, Structures of C-cored and O-cored NHS ester-functionalized MARS probes, each with four isotope combinations on the nitrile bond. **b**, Epr-SRS spectra of the selected eight NHS ester-functionalized MARS probes. **c**, Diffraction-limited immuno-eprSRS imaging of α-tubulin; AU, arbitrary units. Bottom left, magnified image of the region outlined by the white box. Bottom right, epr-SRS signal along the white dotted line cut in the magnified image. **d**, Comparison of immuno-eprSRS with conventional immunofluorescence using the same primary antibody; SNR, signal-to-noise ratio. **e**, Immuno-eprSRS is compatible with common tissue preparations, including frozen tissue of mouse pancreas with glucagon labeled by MARS2176, FFPE tissue of human kidney with vimentin labeled by MARS2200 and PFA-fixed mouse brain tissue with glial fibrillary acidic protein (GFAP) labeled by MARS2145. **f**, A multimodality platform of SRS fluorescence tandem imaging; EOM, electro-optics modulator; DM, dichromic mirror; OB, objective; CO, condenser; PD, photodiode; PMT, photomultiplier tube. **g**, Simultaneous 12-target imaging on mouse cerebellum thin sections. Fluorescence: DNA (DAPI), vesicular glutamate transporter 1 (VGluT1-Alexa Fluor 488, glutamatergic neurons, direct immunolabeling), tyrosine hydroxylase (TH-Alexa Fluor 594, dopaminergic neurons, direct immunolabeling) and F-actin (Phalloidin-Alexa Fluor 647); epr-SRS: neuronal nuclei (NeuN; neurons, MARS2228), α-tubulin-MARS2176 (direct immunolabeling), calbindin (CB; Purkinje neurons, MARS2145), β-III-tubulin (TUBB3; neurons, MARS2200), wheat germ agglutinin (WGA; MARS2242), GABA (γ-aminobutyric acid) B receptor 2 (GABBR2; GABAergic neurons, MARS2212), myelin basic protein (MBP; oligodendrocytes, MARS2188) and GFAP (astrocytes and neural stem cells, MARS2159). Antibody information can be found in Supplementary Table 3; scale bars, 10 μm in **c** and 50 μm in **d**, **e** and **g**.

One-shot 12-color protein imaging with an expanded MARS palette. We next expanded the MARS palette for one-shot multiplex immunolabeling. *N*-hydroxy-succinimidyl-ester (NHS ester) is a common reactive group used to functionalize dyes for subsequent antibody conjugation. Because only four MARS probes were previously synthesized with NHS esters[16] (carbon-cored (C-cored) xanthene structure; Fig. 2a, blue box), we synthesized a new set of NHS ester-functionalized MARS probes that differ in core atoms, ring numbers and isotope combination on nitrile bonds (Supplementary Fig. 1). After examining the resulting SRS spectra, four more MARS probes of an oxygen-cored (O-cored) scaffold were selected (Fig. 2a, red box) based on optimal spectral separation and peak width (Supplementary Fig. 1 and Supplementary Table 2). Together with the original four C-cored probes, we obtained eight

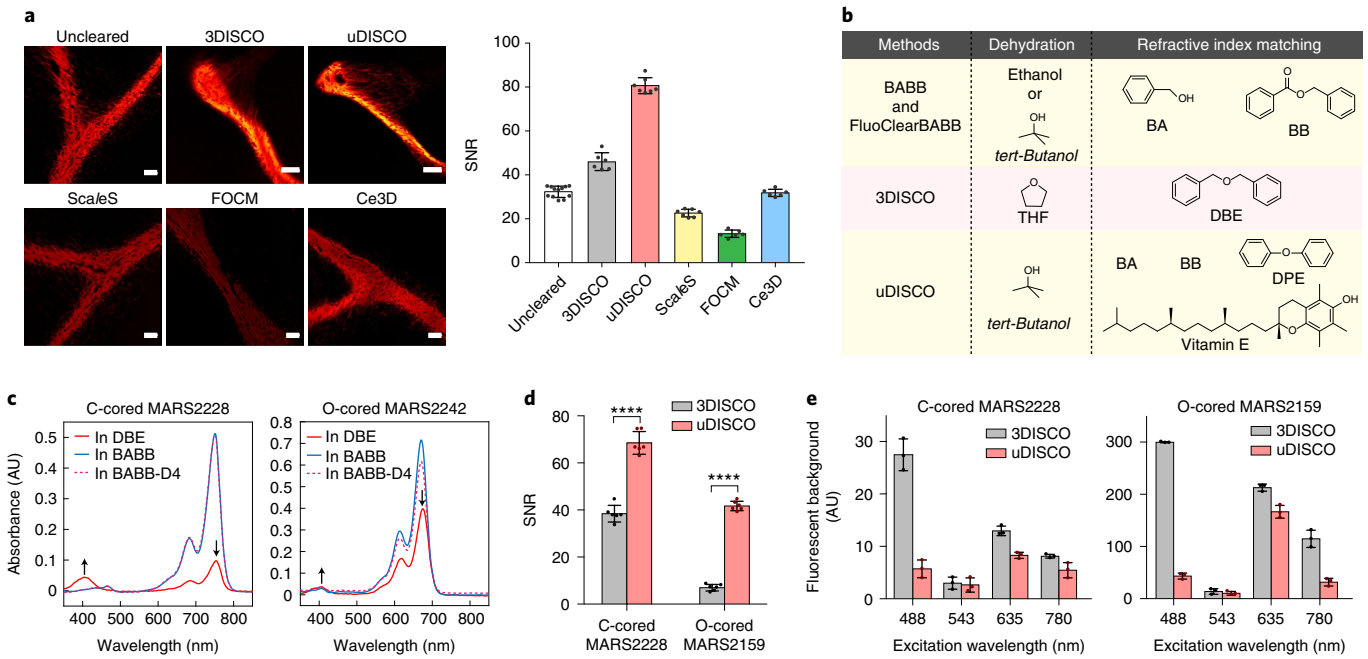

Fig. 3 | Screening and studying tissue-clearing protocols for immuno-eprSRS of MARS probes. a, Screening tissue-clearing protocols for immuno-eprSRS. Left, representative epr-SRS images of MBP (labeled with MARS2176) in cerebellum tissues (40 μm thick) cleared by each protocol; scale bars, 50 μm. Right, quantification of epr-SRS SNRs for different clearing methods ($n = 12$, 6, 7, 7, 6 and 6 regions of interest (ROIs)). **b**, Chemicals used for dehydration and refractive index matching in BABB/FluoClearBABB, 3DISCO and uDISCO. uDISCO utilizes a mixture of benzyl alcohol (BA), benzyl benzoate (BB) and diphenyl ether (DPE) (called BABB-D4) supplemented with vitamin E for refractive index matching; THF, tetrahydrofuran; DBE, dibenzyl ether. **c**, Absorption spectra of MARS probes freshly dissolved in DBE, BABB and BABB-D4 solutions. Arrows indicate a substantial intensity decrease in DBE compared to either BABB or BABB-D4 and the increase of a bluer absorption band; AU, arbitrary units. **d**, Comparison of epr-SRS SNRs between 3DISCO and uDISCO ($n = 6$ ROIs). Cerebellum tissues (100 μm thick) with GFAP labeled by MARS2228 or MARS2159 were used. A two-tailed unpaired *t*-test was used to test for statistical significance; left, $P = 2.2 \times 10^{-7}$, $t = 12$; right, $P = 8.8 \times 10^{-12}$, $t = 35$. **e**, Comparison of postclearing fluorescence background between 3DISCO and uDISCO ($n = 3$ ROIs). The same samples were used as in **d**. Excitation at 780 nm represents a two-photon fluorescence channel excited by a 780-nm pump laser. All data in Fig. 3 are presented as mean ± s.d.

NHS ester-functionalized MARS probes with distinct epr-SRS peaks (Fig. 2b).

Immunostaining of these MARS probes was then verified under epr-SRS (immuno-eprSRS). After conjugating NHS ester-functionalized MARS probes to secondary antibodies, specific protein targets can be visualized inside cells with diffraction-limited resolution (Fig. 2c, Extended Data Fig. 2 and Supplementary Fig. 2). When applied to tissues, immuno-eprSRS is compatible with multiple protein targets (for example, NeuN, GFAP, MBP, MAP2 and CB) and has comparable performance to standard immunofluorescence (Fig. 2d, Extended Data Figs. 3 and 4 and Supplementary Fig. 3). Immuno-eprSRS is applicable to common sample preparations, including paraformaldehyde (PFA)-fixed tissues, formalin-fixed paraffin-embedded (FFPE) tissues and frozen tissues (Fig. 2e). Direct immunostaining with MARS-conjugated primary antibodies also showed good contrast (Extended Data Fig. 3c). Besides immunostaining, MARS-conjugated lectins allowed us to visualize cell membranes and vasculature by targeting glycoproteins (Extended Data Fig. 3d). Together, these results indicate that immuno-eprSRS is generally applicable to imaging various protein targets in diverse tissue types under different sample preparations.

We then pursued simultaneous multiplex immuno-eprSRS imaging. As a feasibility test, two MARS probes with the smallest spectral separation (~12 cm^{-1}, one C-cored and one O-cored) can be used together without cross-talk (Extended Data Fig. 5a), indicating that all eight MARS probes are spectrally separable. Moreover, SRS can be integrated with fluorescence (both confocal and two-photon) as a multimodality platform (Fig. 2f), benefiting in increased multiplexing power and direct access to well-developed fluorescence probes. We then stained mouse cerebellum thin sections and demonstrated 12-plex protein imaging (Fig. 2g, Extended Data Fig. 5b–d and Supplementary Note 1). All targets were imaged with expected patterns similar to the single-channel results (Extended Data Fig. 3). Through established biomarkers, we can identify different cell types, such as cerebellar granule neurons (NeuN), Purkinje neurons (CB), astrocytes (GFAP) and oligodendrocytes (MBP).

Screening and studying tissue-clearing methods for immuno-eprSRS. Next, we sought to develop RADIANT by extending immuno-eprSRS of MARS probes to volumetric imaging. Two-photon excitation of SRS allows for intrinsic 3D optical sectioning and prevents out-of-focus photobleaching (Extended Data Fig. 6). Our main task is thus to identify proper tissue-clearing protocols. While volumetric SRS was recently reported for label-free chemical imaging[29], a urea-based clearing protocol was used to preserve lipids, resulting in a compromised clearing ability in thick tissues (Extended Data Fig. 7a). Additionally, urea is known to disrupt antibody–antigen binding affinity[30] and thus is less ideal for immunostaining. We hence evaluated several immunolabeling-verified and fast clearing approaches, including Sca*l*eS[23], FOCM[24], Ce3D[25], 3DISCO[26] and uDISCO[27]. SNRs of immuno-eprSRS on 40- or 100-μm-thick tissue sections were measured after these clearing procedures, reflecting the joint effect of clearing, staining, probe concentration and stability. We found that DISCO-based methods outperformed others (Fig. 3a), partly due to probe concentration increase mediated by tissue shrinkage. Therefore, we chose DISCO as our basic protocol.

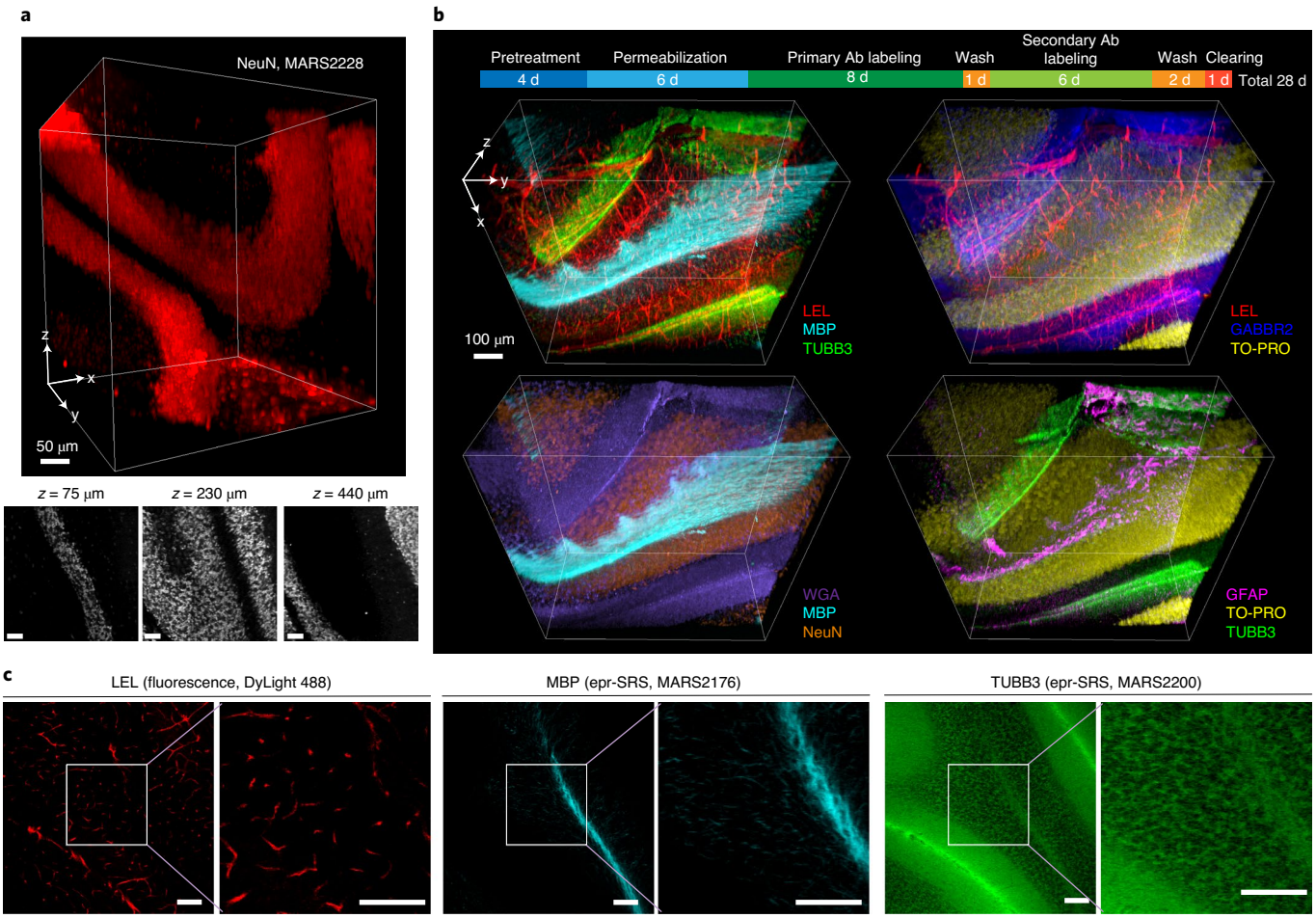

Fig. 4 | Volumetric immuno-eprSRS imaging with uDISCO clearing. a, Volume-rendered image of NeuN (granular neurons) labeled with C-cored MARS2228 in 500-µm-thick cerebellum sections cleared by uDISCO. Single-plane images show good epr-SRS contrast along the whole depth. **b**, One-shot eight-target volume-rendered images of a 500-µm-thick mouse cerebellum section by RADIANT. A typical workflow for tissue sample preparation, staining and clearing is depicted; Ab, antibody. Fluorescence: LEL (*Lycopersicon esculentum* lectin DyLight 488), TO-PRO-3 (TO-PRO; cell nucleus stain); epr-SRS: NeuN (MARS2228), TUBB3 (MARS2200), MBP (MARS2176), GABBR2 (MARS2145), WGA (MARS2242) and GFAP (MARS2159). **c**, Representative single-plane images with zoom-in images at $z = 250$ µm from the 3D data set in **b**; scale bars, 100 µm.

Next, we asked why uDISCO performed better than 3DISCO (Fig. 3a), as tissue shrinkage is similar for both methods. In 3DISCO, the refractive index-matching medium DBE is known to be prone to form peroxides[27] (Fig. 3b and Supplementary Note 2). As shown in the absorption spectra of MARS probes freshly dissolved in the RIMS, a substantial intensity decrease was observed in DBE compared to either BABB or BABB-D4 (BABB:DPE = 4:1 in uDISCO) (Fig. 3b,c). Additionally, a bluer absorption band appeared in DBE, especially for the C-cored probe (Extended Data Fig. 7b). These results collectively suggested the decomposition of MARS probes, likely induced by peroxides formed in DBE. Going from solutions to tissue samples, uDISCO also generated better SNRs in immuno-eprSRS than in 3DISCO (Fig. 3d) and induced less postclearing fluorescence background (Fig. 3e), consistent with the solution results.

By virtue of the chemical stability of MARS probes in uDISCO, we achieved 3D immuno-eprSRS imaging on 500-µm-thick cerebellum sections with good contrast (Fig. 4a and Extended Data Fig. 8). In comparison, the contrast of uncleared samples decreased rapidly over a shallow depth of 50–100 µm (Supplementary Fig. 4). Such single-color success can be readily extended to multiplex epr-SRS imaging thanks to the chemical similarity of all the MARS probes (Fig. 2a). Notably, eight-target volumetric imaging (six SRS and two fluorescence channels) can be performed in one shot by RADIANT with expected patterns along the entire depth for each channel (Fig. 4b,c and Supplementary Fig. 5, magnified views in Fig. 4c), which already breaks the color barrier for thick tissues (Fig. 1).

Development of rDISCO for MARS dyes. Our insight on MARS probe susceptibility to peroxides provides an opportunity to further improve the clearing method. Starting from uDISCO, we found that lowering clearing temperature to 4 °C increased SNR (Fig. 5a), as probe decomposition slows down as temperature decreases[31]. To scavenge peroxides, the uDISCO protocol adds a stable solvent DPE and an antioxidant vitamin E for better preserving of fluorescent proteins[27]. These strategies are also found to work for preserving MARS probes (Fig. 5b). Inspired by these findings, we further screened other common antioxidants in BABB-D4 solution and found that propyl gallate (PG) markedly improved SNR for both O- and C-cored probes (Fig. 5b,c). Indeed, PG is known to be an exceptionally potent antioxidant (~1,000 times more potent than vitamin E)[32–34]. Studying the concentration effect of PG (Fig. 5d), we found that the SNR of MARS dyes plateaued around 1% PG. Together, we finalized this tailored tissue-clearing protocol as BABB-D4 supplemented with 1% PG for clearing at 4 °C and named it rDISCO.

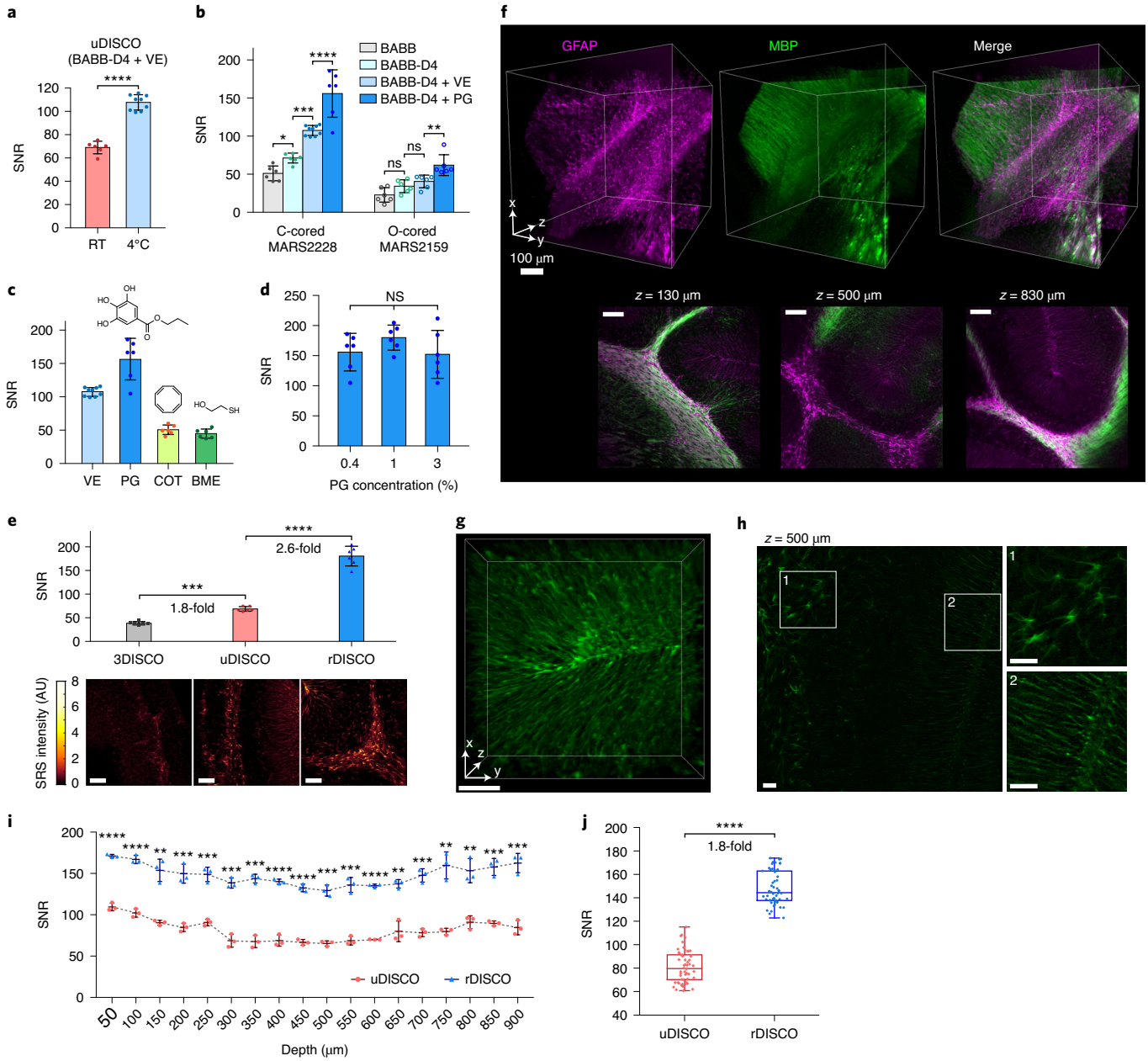

Fig. 5 | Development of MARS probe-tailored rDISCO with improved performance. a, Temperature study with uDISCO. Two-tailed unpaired *t*-test ($n=6$, 9 ROIs), $P=2.3\times10^{-8}$, $t=12$; RT, room temperature; VE, vitamin E. **b-d**, Screening strategies to further scavenge peroxides for better MARS probe preservation. **b**, One-way analysis of variance (ANOVA) followed by Holm–Bonferroni's post hoc test; left, $n=6$, 6, 9 and 6 ROIs; $P=0.039$, 2.7×10^{-4} and 7.8×10^{-6}; right, $n=5$ ROIs, $P=0.066$, 0.31 and 1.6×10^{-3}. **c**, VE, PG, 1,3,5,7-cyclooctatetraene (COT) or β-mercaptoethanol (BME) were added with a concentration of 0.4%. **d**, One-way ANOVA ($n=6$ ROIs), $P=0.29$; NS, not significant. **e**, Comparison of epr-SRS SNRs among 3DISCO, uDISCO and rDISCO. One-way ANOVA followed by Holm–Bonferroni post hoc test ($n=6$ ROIs), $P=7.9\times10^{-4}$ and 1.3×10^{-10}. Representative images for three methods are shown below the bar graph. Mouse cerebellum tissue samples (100 µm thick) with GFAP labeled by MARS2228 or MARS2159 were used in **a**–**e**. MARS2228 was used in **a** and **c**–**e**. In **b**–**d**, clearing was performed at 4 °C. **f**, Volume-rendered images of GFAP (astrocytes, labeled with MARS2145) and MBP (oligodendrocytes, labeled with Alexa Fluor 488) in 1-mm-thick cerebellum sections cleared by rDISCO. Two-color merged single-plane images show good epr-SRS and fluorescence contrast along the whole depth. **g**, Zoomed-in, volume-rendered images of GFAP (labeled with MARS2145) in 1-mm-thick cerebellum sections cleared by rDISCO. **h**, Single-plane images of **g** at 500-µm depth show fine spatial resolution to resolve fibral structures of astrocytes. Left, zoom-in to the regions outlined by the dashed white box. **i**, Comparison of epr-SRS SNRs between rDISCO and uDISCO over the entire thickness of 1-mm-thick samples ($n=3$ ROIs). Two-tailed unpaired *t*-test, all $P<0.0001$. **j**, Comparison of SRS SNR (mean ± s.d.) between uDISCO and rDISCO among all selected depths ($n=18$ depths). Two-tailed paired *t*-test, $P=3.2\times10^{-19}$, $t=28$, mean of ratios on rDISCO/uDISCO is 1.85. All data in Fig. 5 are presented as mean ± s.d.; scale bars, 50 µm in **e**, **g** and **h**.

Finally, we demonstrated RADIANT with rDISCO for improved performance. For immuno-eprSRS on 100-µm sections, rDISCO offered 2.6-fold SNR improvement over uDISCO, which was 1.8-fold better than 3DISCO (Fig. 5e), supporting rDISCO as a valuable improvement. Going to 1-mm-thick cerebellum sections, we labeled GFAP with C-cored MARS probe and made a

comparison between rDISCO and uDISCO (Fig. 5f and Extended Data Fig. 9a). A fluorescence channel targeting MBP was also included as a reference. Zoomed-in images indicate fine spatial resolution of immuno-eprSRS after rDISCO clearing (Fig. 5g,h). Again, rDISCO offered universal SNR improvements over uDISCO for the entire thickness profile (Fig. 5i), which is 1.8-fold on average for all selected depths (Fig. 5j) and ~2-fold for the center region of the tissue (Extended Data Fig. 9b).

One-shot multiplexed imaging of millimeter-scale tissues. Encouraged by the SNR improvement with rDISCO, we accomplished one-shot imaging of 11 different targets in a 1-mm-thick cerebellum section from a developing mouse (postnatal day 15 (P15)) cleared by rDISCO (Fig. 6a and Supplementary Fig. 6). Because all channels were imaged in one round, the resulting images are intrinsically autoaligned in 3D without the need of co-registration correction. The one-shot approach has unique advantages for thick tissues in that antibody staining and imaging can be performed for all targets in one shot, thereby circumventing the key limitations (discussed earlier) associated with cyclic immunofluorescence techniques. The results demonstrated here have extended the imaging depth of state-of-the-art cyclic immunofluorescence imaging (achieving 7–12 colors in 100-μm-thick tissues[13–15]) by tenfold. The improvement is even more (>100-fold) when compared to mass spectrometry-based methods[5,6].

Versatile analysis of segmentation, spatial correlation, cellular composition, 3D distance and network topology. We next showcased the utility of the multiplexed volumetric images in extracting systems information, including regional segmentation, spatial correlation, cellular composition, 3D distance and network topology. First, based on several markers (see Methods for details), we segmented the image into four anatomical layers of the cerebellum, white matter, the granular layer, the Purkinje layer and the molecular layer (Extended Data Fig. 10a). Next, to acquire an overview of protein–protein correlation, we generated the heat maps of Pearson's correlation coefficients between different protein pairs with hierarchical clustering for the four layers (Fig. 6b). The correlation we observed is evidently higher than the random level (Extended Data Fig. 10b). As cerebellar granule cells are the most numerous neurons in the brain with their cell bodies densely packed into the granular layer[35], the neuronal nuclear marker NeuN and the nuclear stain TO-PRO show highly positive correlation in the heat maps and close clustering in the dendrograms of the granular layer and all layers (Fig. 6b). By contrast, two cytoskeleton proteins, the astrocyte-specific GFAP and the neuron-specific TUBB3 (ref. [36]) show negative or close-to-zero correlation in the heat maps and reside far apart in the dendrograms across four anatomical layers (Fig. 6b). These observations capture spatial correlation and clustering with faithful biological meanings.

Cellular composition and 3D distance information can also be obtained. In Fig. 6b (red font), we noticed strong correlation between vimentin and GFAP, two major intermediate filaments for astrocytes, particularly in the white matter ($r = 0.73$). To study vimentin–GFAP correlation in different anatomical layers, we segmented $Vim^+/GFAP^-$, $Vim^-/GFAP^+$ and $Vim^+/GFAP^+$ cells (Fig. 6c) and performed cell compositional analysis (Fig. 6d,e and Extended Data Fig. 10c). In the period of rapid myelination (~P0–P21 for mice), a transition has been reported to occur as vimentin is progressively replaced by GFAP in astrocytes during glial development (Fig. 6c)[37,38]. Hence, $Vim^+/GFAP^-$, $Vim^+/GFAP^+$ and $Vim^-/GFAP^+$ cells will correspond to astrocyte progenitors/radial glia, differentiated astrocytes and mature astrocytes/Bergmann glia[38], respectively (Fig. 6c). Consistently, we found that the majority of astrocytes (that is, $GFAP^+$ cells) coexpress vimentin (Fig. 6e; compare the proportion of $Vim^+/GFAP^+$ cells to that of $Vim^-/GFAP^+$ cells), suggesting an early stage of glial development in the P15 mouse coincident with the time window of myelination[39]. The distance between a cell and its closest blood vessel (cell-to-vessel distance) is a key parameter in the organization and development of the central nervous system, which is intrinsically three-dimensional and has to be assessed from volumetric images. We measured the astrocyte-to-vessel distances (for all $GFAP^+$ cells) in our cerebellum sample as 7.8 ± 0.2 μm (Fig. 6f). This distance is in a similar range to that measured in the mouse somatosensory cortex (6–10 μm) in the literature[40]. Notably, the cell-to-vessel distance is found to exhibit different distributions for three populations of cells, with the mean distances of 8.7 ± 0.2 μm for $Vim^+/GFAP^-$ cells, 5.9 ± 0.2 μm for $Vim^+/GFAP^+$ cells and 17.0 ± 0.6 μm for $Vim^-/GFAP^+$ cells (Fig. 6f,g); the relatively close cell-to-vessel distances for $Vim^+/GFAP^-$ and $Vim^+/GFAP^+$ cells suggests that the coordination and interactions between glial progenitors and blood vessels may peak at an early stage of astrocyte differentiation[41,42]. In particular, the closest association of $Vim^+/GFAP^+$ cells with blood vessels (Fig. 6f,g) and their predominant distribution in white matter (Fig. 6d) echo with the essential functions of astrocytes for the integrity of the blood–brain barrier and white matter vascularization during development[43–45].

Network analysis allows us to explore the underlying architectures and design principles of complex biological systems[46,47]. We analyzed correlation networks of these 11 molecular species for the four anatomical layers (Fig. 6h). First, we calculated two system-level properties of networks: average clustering coefficients and network diameters[46]. The average clustering coefficients range from 0.65 to 0.76 for these five networks. These large, region-independent clustering coefficients indicate modularity of the networks: a group of linked nodes work cooperatively to perform functions[46]. The network diameters are 2 or 3 for these five networks, exhibiting the 'small-world' property[46,47]. Next, we analyzed node importance by calculating the closeness centrality (high centrality implies a central role in the network[48]) and color coded each node with the centrality score, revealing the network of entire space and specific layers (Fig. 6h). For instance, five nodes have high centrality values in the network of all layers: LEL-labeled blood vessels and GFAP-labeled astrocytes maintain the blood–brain barrier and provide nutrients to the nervous tissues[49,50], ConA and GS-II label specific glycoproteins that are involved in cell differentiation and development[51] and

Fig. 6 | RADIANT with rDISCO clearing enables millimeter-scale, highly multiplexed protein imaging. a, Eleven-target volume-rendered images of a 1-mm-thick mouse cerebellum section by RADIANT with rDISCO clearing. Fluorescence: concanavalin A (ConA, Alexa Fluor 350), *Griffonia simplicifolia* lectin (GS-II, Alexa Fluor 488), TUBB3 (Alexa Fluor 594, direct immunolabeling), TO-PRO (cell nucleus stain); epr-SRS: NeuN (MARS2228), LEL (MARS2200), MBP (MARS2176), GABBR2 (MARS2145), WGA (MARS2242), vimentin (Vim, MARS2212) and GFAP (MARS2159). **b**, Pixel-based correlation heat maps for different regions of the cerebellum. The red font indicates strong correlation between GFAP and Vim. **c**, Segmentation of $Vim^+/GFAP^-$, $Vim^-/GFAP^+$ and $Vim^+/GFAP^+$ cells. The scheme shows the transition between three populations during astrocyte differentiation. **d**, Pie charts for cell compositional analysis of three populations in different regions of the cerebellum. **e**, Pie charts for the proportion of the three populations of cells. **f**, Violin plot of cell-to-nearest vasculature distances. One-way ANOVA followed by Holm–Bonferroni's post hoc tests were significant ($n = 3{,}172$, 543, 6,625 and 2,629 cells from a single mouse, $P < 0.0001$). **g**, Histograms of cell-to-nearest vasculature distances of three populations of cells. Averaged distances (mean ± s.e.m.) are shown inside the graph. **h**, Network graph of correlations for different regions of the cerebellum. Centrality is color coded for each node. The node size is directly proportional to the number of edges connected to each node; scale bars, 100 μm.

GABBR2 is a key inhibitory receptor for synaptic transmission[52]. Of note, the node TUBB3 exhibits a high centrality score only in the Purkinje layer in contrast to its low centrality scores in the other three layers. This distinct topology of TUBB3 suggests its special role for Purkinje cells. Indeed, TUBB3 was the only β-tubulin isotype expressed in Purkinje cells, with an essential role in axon guidance and maintenance[53,54]. Taken together, mapping 3D spatially resolved correlation networks of proteins has gained insight into the organizational principles of complex tissues. Such analysis may be extended to identify potential molecular targets for diagnostic and therapeutic applications.

Discussion

High-content, large-context protein imaging is becoming increasingly critical in life science. Toward this goal, extensive efforts have been devoted to developing multiplexed protein imaging in large 3D

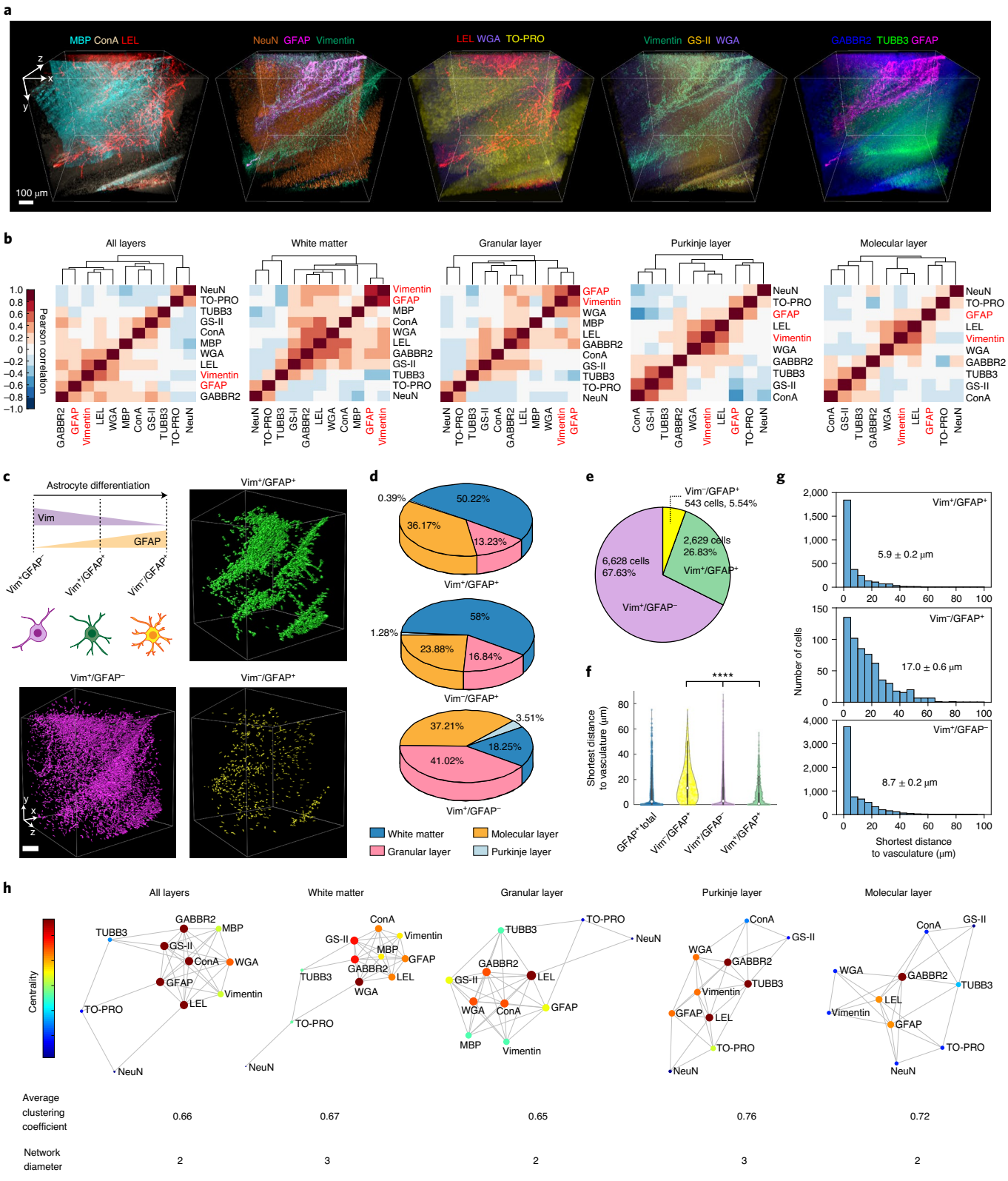

biological systems. However, current protein-imaging methods are constrained by a general trade-off between the achievable content (that is, high multiplexing) and context (that is, thick samples). As we summarize in Fig. 1, all the existing multiplexed protein-imaging techniques are confined to shallow depths (<100 μm; that is, poor context), whereas protein imaging in thick tissues (>100 μm) cannot exceed approximately five colors (that is, poor content) and is limited by the fluorescent 'color barrier'. Due to this content–context trade-off, highly multiplexed volumetric protein imaging remains challenging.

Different from these precedents, our approach is a one-shot optical method without the compromise between depth and multiplexity (Supplementary Table 4) by leveraging innovations in coherent Raman microscopy, probe chemistry and tissue engineering. Specifically, we exploited the coupling between tissue-clearing technology and epr-SRS microscopy, the most sensitive vibrational imaging modality to date. After observing the interfering background from the tissue-clearing reagents with conventional Raman dyes, we reported new bioorthogonal vibrational probes for immuno-eprSRS, offering good detectability (comparable to standard immunofluorescence), fine spatial resolution, general sample compatibility and scalable multiplexity. In addition, after screening and studying common tissue-clearing methods for volumetric immuno-eprSRS, we developed a MARS probe-tailored tissue-clearing method rDISCO. Combining these developments together, we have achieved one-shot multiplex (>10) protein imaging within a single tissue of millimeter thickness. Systematic analyses of the images showcased the utility in extracting regional segmentation, spatial correlation, cellular composition, 3D distance and network topology. Conclusively, our RADIANT approach of coupling one-shot epr-SRS microscopy of MARS probes with tailored tissue clearing circumvents practical complexity in cyclic methods and largely improves the throughput, thereby opening up a new territory for high-content, large-context protein imaging (Fig. 1).

Future optimizations of RADIANT reside along several fronts. First, penetration depth and staining uniformity of current passive antibody permeation are suboptimal and dependent on the specimen size and abundance of target proteins, preventing our demonstration going beyond 1-mm thickness. Recent innovations on rapid and uniform immunolabeling using facilitated transport[13,55] are promising to extend the depth and greatly shorten the entire pipeline. Second, a relatively long pixel dwell time (60 μs) makes the net acquisition time of Fig. 6a about 4 h. Explorations on in situ signal amplification techniques[56,57] are expected to substantially boost the imaging speed and throughput. Third, current multiplexity of 11 channels is jointly limited by the availability of source species of secondary antibodies and resolvable Raman probes. Further increased plex (>20) can be foreseen through introducing functionalized polyyne-based Raman probes[58] as well as systematic validation of a library of Raman probe-conjugated primary antibodies. Fourth, pursing RNA and DNA as the targeted molecules will presumably make RADIANT a spatial-resolved pan-omics tool.

Our high-content, large-context protein-imaging approach provides intrinsic advantages for molecular profiling in intact tissues as it is non-destructive, cycle free and registration free. Notably, a fully integrated multimodal SRS/fluorescence research microscope similar to the system in this work has already been commercialized (Supplementary Note 1), providing direct instrumental accessibility to biomedical researchers. Overall, we envision that RADIANT will be valuable for deciphering complex biological systems, such as building tissue atlases, phenotyping tumor microenvironments and profiling brain circuits.

Online content

Any methods, additional references, Nature Research reporting summaries, source data, extended data, supplementary information, acknowledgements, peer review information; details of author contributions and competing interests; and statements of data and code availability are available at https://doi.org/10.1038/s41587-021-01041-z.

Received: 3 January 2021; Accepted: 29 July 2021;
Published online: 04 October 2021

References

1. Luo, C. et al. Single-cell methylomes identify neuronal subtypes and regulatory elements in mammalian cortex. *Science* **357**, 600–604 (2017).
2. Lichtman, J. W. & Denk, W. The big and the small: challenges of imaging the brain's circuits. *Science* **334**, 618–623 (2011).
3. Tsurui, H. et al. Seven-color fluorescence imaging of tissue samples based on Fourier spectroscopy and singular value decomposition. *J. Histochem. Cytochem.* **48**, 653–662 (2000).
4. Cutrale, F. et al. Hyperspectral phasor analysis enables multiplexed 5D in vivo imaging. *Nat. Methods* **14**, 149–152 (2017).
5. Angelo, M. et al. Multiplexed ion beam imaging of human breast tumors. *Nat. Med.* **20**, 436–442 (2014).
6. Giesen, C. et al. Highly multiplexed imaging of tumor tissues with subcellular resolution by mass cytometry. *Nat. Methods* **11**, 417–422 (2014).
7. Gerdes, M. J. et al. Highly multiplexed single-cell analysis of formalin-fixed, paraffin-embedded cancer tissue. *Proc. Natl Acad. Sci. USA* **110**, 11982–11987 (2013).
8. Lin, J.-R. et al. Highly multiplexed immunofluorescence imaging of human tissues and tumors using t-CyCIF and conventional optical microscopes. *eLife* **7**, e31657 (2018).
9. Gut, G., Herrmann, M. D. & Pelkmans, L. Multiplexed protein maps link subcellular organization to cellular states. *Science* **361**, eaar7042 (2018).
10. Goltsev, Y. et al. Deep profiling of mouse splenic architecture with CODEX multiplexed imaging. *Cell* **174**, 968–981 (2018).
11. Chung, K. et al. Structural and molecular interrogation of intact biological systems. *Nature* **497**, 332–337 (2013).
12. Renier, N. et al. iDISCO: a simple, rapid method to immunolabel large tissue samples for volume imaging. *Cell* **159**, 896–910 (2014).
13. Murray, E. et al. Simple, scalable proteomic imaging for high-dimensional profiling of intact systems. *Cell* **163**, 1500–1514 (2015).
14. Ku, T. et al. Multiplexed and scalable super-resolution imaging of three-dimensional protein localization in size-adjustable tissues. *Nat. Biotechnol.* **34**, 973–981 (2016).
15. Park, Y.-G. et al. Protection of tissue physicochemical properties using polyfunctional crosslinkers. *Nat. Biotechnol.* **37**, 73–83 (2019).
16. Wei, L. et al. Super-multiplex vibrational imaging. *Nature* **544**, 465–470 (2017).
17. Kawata, S., Ichimura, T., Taguchi, A. & Kumamoto, Y. Nano-Raman scattering microscopy: resolution and enhancement. *Chem. Rev.* **117**, 4983–5001 (2017).
18. Wei, L. & Min, W. Electronic preresonance stimulated Raman scattering microscopy. *J. Phys. Chem. Lett.* **9**, 4294–4301 (2018).
19. Miao, Y., Shi, L., Hu, F. & Min, W. Probe design for super-multiplexed vibrational imaging. *Phys. Biol.* **16**, 041003 (2019).
20. Richardson, D. S. & Lichtman, J. W. Clarifying tissue clearing. *Cell* **162**, 246–257 (2015).
21. Ueda, H. R. et al. Tissue clearing and its applications in neuroscience. *Nat. Rev. Neurosci.* **21**, 61–79 (2020).
22. Dougan, J. A. & Faulds, K. Surface enhanced Raman scattering for multiplexed detection. *Analyst* **137**, 545–554 (2012).
23. Hama, H. et al. ScaleS: an optical clearing palette for biological imaging. *Nat. Neurosci.* **18**, 1518–1529 (2015).
24. Zhu, X. et al. Ultrafast optical clearing method for three-dimensional imaging with cellular resolution. *Proc. Natl Acad. Sci. USA* **116**, 11480–11489 (2019).
25. Li, W., Germain, R. N. & Gerner, M. Y. Multiplex, quantitative cellular analysis in large tissue volumes with clearing-enhanced 3D microscopy (Ce3D). *Proc. Natl Acad. Sci. USA* **114**, E7321–E7330 (2017).
26. Ertürk, A. et al. Three-dimensional imaging of solvent-cleared organs using 3DISCO. *Nat. Protoc.* **7**, 1983–1995 (2012).
27. Pan, C. et al. Shrinkage-mediated imaging of entire organs and organisms using uDISCO. *Nat. Methods* **13**, 859–867 (2016).
28. Hu, F., Shi, L. & Min, W. Biological imaging of chemical bonds by stimulated Raman scattering microscopy. *Nat. Methods* **16**, 830–842 (2019).
29. Wei, M. et al. Volumetric chemical imaging by clearing-enhanced stimulated Raman scattering microscopy. *Proc. Natl Acad. Sci. USA* **116**, 6608–6617 (2019).
30. Bata, J. E., Gyenes, L. & Sehon, A. H. The effect of urea of antibody–antigen reactions. *Immunochemistry* **1**, 289–293 (1964).
31. Qi, Y. et al. FDISCO: advanced solvent-based clearing method for imaging whole organs. *Sci. Adv.* **5**, eaau8355 (2019).
32. Hahn, C. et al. High-resolution imaging of fluorescent whole mouse brains using stabilised organic media (sDISCO). *J. Biophotonics* **12**, e201800368 (2019).

33. Medina, M. E., Iuga, C. & Alvarez-Idaboy, J. R. Antioxidant activity of propyl gallate in aqueous and lipid media: a theoretical study. *Phys. Chem. Chem. Phys.* **15**, 13137–13146 (2013).
34. Haseloff, R. F., Blasig, I. E., Meffert, H. & Ebert, B. Hydroxyl radical scavenging and antipsoriatic activity of benzoic acid derivatives. *Free Radic. Biol. Med.* **9**, 111–115 (1990).
35. Llinás, R. R., Walton, K. D. & Lang, E. J. in *The Synaptic Organization of the Brain* 5th edn (ed Shepherd G. M.) Ch. 7 (Oxford University Press., 2004).
36. Katsetos, C. D., Herman, M. M. & Mörk, S. J. Class III β-tubulin in human development and cancer. *Cell Motil. Cytoskeleton* **55**, 77–96 (2003).
37. Schnitzer, J., Franke, W. W. & Schachner, M. Immunocytochemical demonstration of vimentin in astrocytes and ependymal cells of developing and adult mouse nervous system. *J. Cell Biol.* **90**, 435–447 (1981).
38. Bovolenta, P., Liem, R. K. H. & Mason, C. A. Development of cerebellar astroglia: transitions in form and cytoskeletal content. *Dev. Biol.* **102**, 248–259 (1984).
39. Molofsky, A. V. et al. Astrocytes and disease: a neurodevelopmental perspective. *Genes Dev.* **26**, 891–907 (2012).
40. McCaslin, A. F. H., Chen, B. R., Radosevich, A. J., Cauli, B. & Hillman, E. M. C. In vivo 3D morphology of astrocyte—vasculature interactions in the somatosensory cortex: implications for neurovascular coupling. *J. Cereb. Blood Flow Metab.* **31**, 795–806 (2010).
41. Zerlin, M. & Goldman, J. E. Interactions between glial progenitors and blood vessels during early postnatal corticogenesis: blood vessel contact represents an early stage of astrocyte differentiation. *J. Comp. Neurol.* **387**, 537–546 (1997).
42. Paredes, I., Himmels, P. & Ruiz de Almodóvar, C. Neurovascular communication during CNS development. *Dev. Cell* **45**, 10–32 (2018).
43. Liedtke, W. et al. GFAP is necessary for the integrity of CNS white matter architecture and long-term maintenance of myelination. *Neuron* **17**, 607–615 (1996).
44. Ishibashi, T. et al. Astrocytes promote myelination in response to electrical impulses. *Neuron* **49**, 823–832 (2006).
45. Lundgaard, I., Osório, M. J., Kress, B. T., Sanggaard, S. & Nedergaard, M. White matter astrocytes in health and disease. *Neuroscience* **276**, 161–173 (2014).
46. Barabási, A.-L. & Oltvai, Z. N. Network biology: understanding the cell's functional organization. *Nat. Rev. Genet.* **5**, 101–113 (2004).
47. Albert, R. Scale-free networks in cell biology. *J. Cell Sci.* **118**, 4947 (2005).
48. Jeong, H., Mason, S. P., Barabási, A. L. & Oltvai, Z. N. Lethality and centrality in protein networks. *Nature* **411**, 41–42 (2001).
49. Abbott, N. J., Rönnbäck, L. & Hansson, E. Astrocyte–endothelial interactions at the blood–brain barrier. *Nat. Rev. Neurosci.* **7**, 41–53 (2006).
50. Freeman, M. R. & Rowitch, D. H. Evolving concepts of gliogenesis: a look way back and ahead to the next 25 years. *Neuron* **80**, 613–623 (2013).
51. Gulati, A. K., Zalewski, A. A., Sharma, K. B., Ogrowsky, D. & Sohal, G. S. A comparison of lectin binding in rat and human peripheral nerve. *J. Histochem. Cytochem.* **34**, 1487–1493 (1986).
52. Bettler, B., Kaupmann, K., Mosbacher, J. & Gassmann, M. Molecular structure and physiological functions of GABAB receptors. *Physiol. Rev.* **84**, 835–867 (2004).
53. Burgoyne, R. D., Cambray-Deakin, M. A., Lewis, S. A., Sarkar, S. & Cowan, N. J. Differential distribution of β-tubulin isotypes in cerebellum. *EMBO J.* **7**, 2311–2319 (1988).
54. Tischfield, M. A. et al. Human TUBB3 mutations perturb microtubule dynamics, kinesin interactions, and axon guidance. *Cell* **140**, 74–87 (2010).
55. Yun, D. H. et al. Ultrafast immunostaining of organ-scale tissues for scalable proteomic phenotyping. Preprint at *bioRxiv* https://doi.org/10.1101/660373 (2019).
56. Saka, S. K. et al. Immuno-SABER enables highly multiplexed and amplified protein imaging in tissues. *Nat. Biotechnol.* **37**, 1080–1090 (2019).
57. Lin, R. et al. A hybridization-chain-reaction-based method for amplifying immunosignals. *Nat. Methods* **15**, 275–278 (2018).
58. Hu, F. et al. Supermultiplexed optical imaging and barcoding with engineered polyynes. *Nat. Methods* **15**, 194–200 (2018).

Methods

Protein–MARS probe conjugation. NHS ester-functionalized MARS probes were stored at a concentration of 10 mM in DMSO at −20 °C protected from light and moisture. To perform protein–dye conjugation, dye solutions were first diluted in DMSO to a concentration of 2 mg ml^{-1}. Conjugation buffer was prepared as 0.1 M $NaHCO_3$ in PBS buffer with the pH adjusted to 8.3. Highly cross-absorbed secondary antibodies were buffer exchanged and concentrated to 2 mg ml^{-1} in the conjugation buffer. A 50-µl dye–NHS solution was slowly added to a 0.5-ml secondary antibody solution with stirring. For primary antibody labeling, the protein concentration was adjusted to 1 mg ml^{-1}, and the molar ratio of dye:protein was usually 10–15. Lectins were first dissolved in conjugation buffer at 2 mg ml^{-1}. For WGA labeling, a 10-µl 2 mg ml^{-1} dye–NHS solution was added to a 0.5-ml 2 mg ml^{-1} WGA solution. For LEL labeling, a 25-µl 2 mg ml^{-1} dye–NHS solution was added to a 0.5-ml 2 mg ml^{-1} LEL solution. Reactions were all incubated at room temperature for 1 h with constant mild stirring. Labeled proteins were further separated from unreacted dyes by gel permeation chromatography using Sephadex G-25 (G25150, Sigma) resins with a column that was 1 cm in diameter and over 12 cm in length. Purified protein solution was centrifuged to remove potential precipitates and further concentrated with Amicon Ultra centrifugal filters (UFC501096, EMD, Millipore). A final concentration of ~2 mg ml^{-1} protein solution (for secondary antibodies and lectins) was prepared in stocking buffer (30% glycerol and 5 mM sodium azide in PBS) and stored at −20 °C. The degree of labeling (that is, dye-to-protein ratio) was measured by ultraviolet-visable (UV-Vis) spectrum using a Tecan Infinite 200 Reader with a NanoQuant Plate. The degree of labeling on secondary antibodies is about 3.

Cell culture. Human HeLa (ATCC, CCL-2) and COS-7 (ATCC, CRL-1651) cells were cultured in DMEM (Invitrogen, 11965) supplemented with 10% fetal bovine serum (FBS; Invitrogen, 10082) and 1× penicillin/streptomycin (Invitrogen, 15140). Human MCF7 (ATCC, HTB-22) cells were cultured in EMEM (ATCC, 30-2003) supplemented with 10% FBS and 1× penicillin/streptomycin.

Mouse sample preparation. *Brain tissues.* The animal experimental protocol (AC-AABD1552) was approved by the Institutional Animal Care and Use Committee (IACUC) at Columbia University. Wild-type male and female mice (C57BL/6, 15–25 d old, Jackson Laboratory) were fully anesthetized using isoflurane, killed with cervical displacement and immediately perfused with 4% paraformaldehyde (PFA) in PBS transcranially. The brain was extracted and fixed in 4% PFA in PBS at 4 °C for 24 h. After that, the brain was immersed in PBS at 4 °C for 24 h to remove PFA. The cerebellum was embedded in 7% agarose gel and sectioned into 40-µm-, 100-µm-, 500-µm- and 1-mm-thick coronal slices using a vibratome (VT1000S, Leica). Agarose was removed by a tweezer before staining.

Pancreas tissues. All animal procedures were performed under protocols approved by the IACUC of Colorado Anschutz Medical campus (00024). Wild-type male and female mice (C57BL/6, 8–12 weeks old, Jackson Laboratory) were anesthetized by intraperitoneal injection of ketamine (80 mg kg^{-1}) and xylazine (16 mg kg^{-1}) until no longer reactive to toe pinch. Pancreata were dissected and mice were then killed by exsanguination and/or bilateral thoracotomy. Pancreata were fixed in PFA (4% in PBS) at 4 °C with rocking for 16–20 h, washed in 4 °C PBS to remove PFA and embedded in optimal cutting temperature (OCT) compound blocks. Sections (8 µm) were then taken for staining.

SRS and fluorescence integrated imaging platform. SRS and fluorescence imaging were performed on an inverted laser-scanning microscope (Olympus FV1200) using a ×25 water immersion objective lens (Olympus XLPlan N, 1.05-NA, MP, working distance = 2 mm).

For SRS imaging, two synchronized 6-ps lasers (called pump and Stokes beams) with an 80-MHz repetition rate were provided by a picoEmerald system from Applied Physics & Electronic. The pump beam is tunable from 720–990 nm through both temperature control of the non-linear crystal and a Lyot filter. The Stokes beam was fixed at 1,064.2 nm. The intensity of the Stokes beam was modulated sinusoidally by a built-in EOM at 8 MHz with a modulation depth of more than 90%. Spatially and temporally overlapped pump and Stokes beams were coupled into the laser-scanning microscope. After passing through the specimens, forward-going pump and Stokes beams were collected with an infrared-coated oil condenser (1.4-NA, Olympus). Stokes beams were completely filtered with two high optical density bandpass filters (890/220 CARS, Chroma Technology), and transmitted pump beams were detected by a large-area (10 mm × 10 mm) Si photodiode (FDS1010, Thorlabs). The output current of the photodiode was then sent to a fast lock-in amplifier (HF2LI, Zurich Instruments) for signal demodulation. For immuno-eprSRS imaging, the laser power was set as $P_{pump} = 17$ mW and $P_{Stokes} = 50$ mW for C-cored MARS probes and as $P_{pump} = 17$ mW and $P_{Stokes} = 67$ mW for O-cored MARS probes. SRS images were generated through Kalman filtering of 10–30 serial frames with a pixel dwell time of 4 µs. The time constants of the lock-in amplifier were chosen as 2–4 µs. Pixel sizes were chosen as about 0.25–1 µm. For volumetric imaging, the step size in z was 5 µm.

For two-photon fluorescence, DAPI dye or Alexa Fluor 350 were excited by the SRS pump laser at 760 nm. The backward fluorescence was detected after passing through a 690-nm short-pass filter, reflected by a 570-nm long-pass dichroic mirror with a collection band of 410–490 nm. For confocal fluorescence, the green channel was excited by an argon laser (488 nm) with a collection band of 505–520 nm, the red channel was excited by an HeNe(G) laser (543 nm) with a collection band of 560–620 nm and the far-red channel was excited by an LD laser (635 nm) with a collection band of 655–755 nm. A multichannel photomultiplier tube (PMT) was used for fluorescence detection. Pixel sizes were chosen as about 0.25–1 µm, and pixel dwell times were set as 2–4 µs.

Immuno-eprSRS staining on thin tissue sections. For PFA-fixed mouse cerebellum thin sections, 40-µm-thick sections from P15–P40 young mice were used. The staining was performed on the floating tissues in a four-well plate. Samples were permeabilized and blocked with blocking buffer (5% donkey serum, 0.5% Triton X-100 in PBS) at room temperature for 30 min. After blocking, samples were incubated with primary antibody (typical dilution, 1:100) in staining buffer (2% donkey serum, 0.5% Triton X-100 in PBS) at 4 °C for 1–2 d, followed by washing at room temperature for 5–10 min in PBS with 0.5% Triton X-100 (0.5% PBST) three times. Samples were then blocked in blocking buffer for 30 min and incubated with MARS-conjugated secondary antibody (typical dilution, 1:100) in staining buffer at 4 °C for 1–2 d. After staining, the samples were washed at room temperature for 5–10 min in 0.5% PBST three times.

Frozen mouse pancreatic tissue slides were stored at −80 °C. Specimens were first equilibrated to room temperature and held in PBS buffer before staining. The staining processes were performed on slides with a similar protocol as described above for PFA tissues with the following changes. A Triton X-100 concentration of 0.3% was used for blocking buffer, staining buffer and sample washing. The incubation time for both primary and secondary antibodies was 18 h.

The FFPE human kidney slice used in this study was purchased from Biomax (HuFPT072). FFPE tissue slides were first baked at 60 °C for 10 min. Samples were sequentially placed in the following solutions (in a 50-ml Falcon tube) for 3 min each time at room temperature with mild shaking for deparaffinization and rehydration: (1) xylene two times, (2) ethanol two times, (3) 95% (vol/vol) ethanol in deionized water two times, (4) 70% (vol/vol) ethanol in deionized water two times, (5) 50% (vol/vol) ethanol in deionized water one time and (6) deionized water one time. For antigen retrieval, the specimen was first transferred into a glass jar filled with 20 mM sodium citrate (pH 8.0) at 100 °C, followed by a quick transfer of the jar to a 60 °C incubation chamber for 45 min. After that, the specimen was washed at room temperature with deionized water for 5 min. The staining processes followed the same protocol as the frozen tissues.

For imaging specimen preparation, PFA-fixed tissue sections were transferred to Superfrost glass slides, and all specimens were mounted in ProLong Gold antifade (ThermoFisher, P10144) with a glass coverslip and secured with nail polish.

Twelve-target mouse cerebellum imaging. *Staining.* See Fig. 2g and Extended Data Fig. 5c,d. The staining processes followed the sample protocol as PFA-fixed thin tissue sections above with three rounds of antibody incubation. The following antibodies were used in the first round: anti-NeuN (rabbit, dilution 1:50), anti-β-III-tubulin (chicken, dilution 1:50), anti-calbindin (mouse, dilution 1:40), anti-GABBR2 (guinea pig, dilution 1:40), anti-MBP (rat, dilution 1:20), anti-GFAP (goat, dilution 1:50) and MARS2242-conjugated WGA (1:50). The following antibodies were used in the second round: MARS2228-conjugated donkey anti-rabbit IgG, MARS2220-conjugated donkey anti-chicken IgY, MARS2145-conjugated donkey anti-mouse IgG, MARS2212-conjugated donkey anti-guinea pig IgG, MARS2188-conjugated donkey anti-rat IgG and MARS2159-conjugated donkey anti-goat IgG with a dilution of 1:50. The following antibodies were used for the third round: Alexa Fluor 596-conjugated anti-TH (mouse, dilution 1:50), Alexa Fluor 488-conjugated anti-VGluT1 (mouse, dilution 1:50) and MARS2176-conjugated anti-α-tubulin (mouse, 0.5 mg ml^{-1}, dilution 1:40). Between the second and third rounds of antibody incubation, samples were further blocked in 5% normal mouse serum and 0.5% Triton X-100 in PBS at room temperature for 1 h. The specimens were further stained with NucBlue and Phalloidin-Alexa Fluor 647 and embedded in ProLong Gold antifade medium for imaging.

Spectral unmixing. A linear combination algorithm was applied on multiplexed epr-SRS data to remove potential cross-talk between different channels[16]. For N-channel epr-SRS measurement with N MARS probes ($N = 8$ here), measured signals (S) can be expressed as $S = MC$, where C is the MARS probe concentrations, and M is an $N \times N$ matrix determined by Raman cross sections of MARS probes. Matrix M was measured experimentally on single-color immuno-eprSRS labeled with different MARS probes. MARS probe concentrations were therefore determined using $C = M^{-1}S$.

Clearing method screening for immuno-eprSRS on MARS probes. *Staining.* Samples were first washed with 0.2% PBST at room temperature on a shaking platform for 1 h twice followed by incubation in 20% DMSO and 0.2% Triton X-100 in PBS at 37 °C on a shaking platform overnight. The tissues were incubated in 0.1% Tween-20, 0.1% Triton X-100, 0.1% deoxycholate, 0.1% NP-40 and 20% DMSO in PBS at 37 °C on a shaking platform overnight. The tissues were washed with 0.2% PBST at room temperature on a shaking platform for 1 h twice. The tissues were permeabilized with 0.5% PBST at 37 °C on a shaking platform

overnight and then permeabilized and blocked with blocking buffer (5% donkey serum, 0.5% Triton X-100 in PBS) at 37 °C on a shaking platform for 3 d. The tissues were incubated with anti-MBP antibody (rat, dilution 1:20) or anti-GFAP antibody (goat, dilution 1:40) diluted in staining buffer (2% donkey serum, 0.5% Triton X-100 in PBS) at 37 °C on a shaking platform for 2 d and then washed with 0.5% PBST at 37 °C on a shaking platform for 1 d (the solution was changed several times in between). The tissues were then incubated with MARS2200-conjugated donkey anti-rat IgG antibody (dilution 1:50), MARS2228-conjugated donkey anti-goat IgG antibody (dilution 1:40) or MARS2159-conjugated donkey anti-goat IgG antibody (dilution 1:40) diluted in staining buffer at 37 °C on a shaking platform for 2 d. The tissues were washed with 0.5% PBST at 37 °C on a shaking platform for 3 h. The tissues were then incubated in PBS at 4 °C overnight. After that, the tissues were cleared with published tissue-clearing methods, including Sca*l*eS[23], FOCM[24], Ce3D[25], 3DISCO[26] and uDISCO[27] as previously described, or with different tissue-clearing conditions explored in this work. The cleared tissues were mounted on glass slides in a pool created by dental cement and filled with the corresponding RIMs and covered with a glass coverslip for SRS imaging.

Quantification. The SNRs of the raw images were quantified as the main criterion to evaluate different tissue-clearing methods. Specifically, the SNR was calculated as (intensity of the labeled structure per cell − intensity of the background)/s.d. of the background. The background was measured from the same tissue where no stained pattern appears under the same imaging condition. Thus, the noise is composed of both instrumental noise and sample noise. The SNRs of multiple regions of interest were quantified and presented as mean ± s.d. ROIs were manually selected with correct localization pattern and from a similar depth.

rDISCO clearing procedure. The immuno-labeled tissues were first dehydrated in a *tert*-butanol/deionized water series as 30% (vol/vol), 50% (vol/vol), 70% (vol/vol), 80% (vol/vol) and 90% (vol/vol) *tert*-butanol for 2 h each at room temperature on a rotator. The tissues were then incubated in 96% (vol/vol) *tert*-butanol in water at room temperature on a rotator overnight. The tissues were incubated in pure *tert*-butanol at room temperature on a rotator for 2 h. The tissues were incubated in the RIMS, which was prepared by mixing BABB (BA and BB were mixed at a ratio of 1:2 and purified by column chromatography using aluminum oxide) with diphenyl ether at a ratio of 4:1 and adding 1% propyl gallate (wt/vol) at 4 °C for 2 h. The tissues were then mounted in the same RIMS for SRS imaging.

Preprocessing and staining of thick tissue sections. Sample preprocessing. The preprocessing protocol was adapted from the sample pretreatment procedures in iDISCO[12]. For initial processing, tissue samples were washed with 0.2% PBST at room temperature on a shaking platform for 1 h twice and then incubated in 20% DMSO in 0.2% PBST at 37 °C on a shaking platform overnight. The tissues were then incubated in 0.1% Tween-20, 0.1% Triton X-100, 0.1% deoxycholate, 0.1% NP-40 and 20% DMSO in PBS at 37 °C on a shaking platform overnight. Tissues were washed with 0.2% PBST at room temperature on a shaking platform for 1 h twice and then further permeabilized with 0.5% PBST at 37 °C on a shaking platform overnight followed by blocking/permeabilization with 5% donkey serum in 0.5% PBST at 37 °C on a shaking platform for 6 d (the solution was changed once after 3 d). After this, the tissue slices were ready for immunostaining.

Thick sample staining. The staining processes followed similar procedures as thin tissue with varied time and probe concentrations. Detailed descriptions can be found in the Supplementary Methods.

Three-dimensional reconstruction. Raw volumetric data were unmixed into specific channels using the linear combination algorithm as mentioned above. A median filter was applied to the unmixed images for noise reduction. A Fiji plugin[59] was then applied to the images for attenuation correction. The open radius was set to 0.5. After correction, the images were volume rendered in the mode of maximal intensity projection using Imaris (Bitplane).

Three-dimensional segmentation and quantitative analyses. Raw volumetric data went through linear unmixing, noise reduction with a median filter and attenuation correction as mentioned above. Based on the channels of MBP, NeuN and GABBR2, the image was segmented manually using the 'Contour' tool in Imaris into four anatomical layers: white matter, the granular layer, the Purkinje layer and the molecular layer. Segmentation results were exported from Imaris as four binary masks. After the image was median filtered using a radius of 2 pixels and thresholded with Otsu's method, Pearson correlation coefficients were calculated between specific protein channels in the four layers and presented as heat maps using custom-written MATLAB (MathWorks) scripts. As the MBP channel had no signals in the Purkinje layer and the molecular layer after thresholding, correlation analysis was performed with the rest of the ten channels without the MBP channel for these two layers (Fig. 6b). Vimentin$^+$ and GFAP$^+$ cells were segmented using Imaris. The GFAP$^+$ cells that did not touch vimentin$^+$ cells were defined as Vim$^-$/GFAP$^+$ cells. The vimentin$^+$ cells that did not touch GFAP$^+$ cells were defined as Vim$^+$/GFAP$^-$ cells. The GFAP$^+$ cells that touched vimentin$^+$ cells and the vimentin$^+$ cells that touched GFAP$^+$ cells were merged into one channel and segmented as Vim$^+$/GFAP$^+$ cells. The proportions of Vim$^-$/GFAP$^+$, Vim$^+$/GFAP$^-$ and Vim$^+$/GFAP$^+$ cells in the four layers were quantified using the shortest distances to the segmented four layers (a negative shortest distance meant the cell was inside the layer). Cells that spanned multiple layers were excluded from this analysis). Blood vessels were segmented from the LEL channel using Imaris. Shortest distances from Vim$^-$/GFAP$^+$, Vim$^+$/GFAP$^-$ and Vim$^+$/GFAP$^+$ cells to the blood vessels were quantified using Imaris. Correlation-based network graphs were plotted in the four layers using custom-written MATLAB (MathWorks) scripts. Specifically, the 'graph' function in MATLAB was used with Pearson correlation coefficients as the input. Self-loops and negative correlation coefficients were discarded. Closeness node centrality was calculated with the 'centrality' function and color coded in each node. The node size was set to be directly proportional to the degree of each node. Network diameters were calculated with the 'distances' function. Average clustering coefficients were calculated with the 'clusteringcoef' function in the Graph package[60].

Statistics and reproducibility. Statistical analysis was performed using GraphPad Prism 7 and OriginPro 8. Data are presented as mean ± s.d. or mean ± s.e.m. with statistical significance if required (not significant $P \geq 0.05$, $^*P < 0.05$, $^{**}P < 0.01$, $^{***}P < 0.001$, $^{****}P < 0.0001$). In Fig. 5i, $P = 3.0 \times 10^{-5}$, 9.3×10^{-5}, 1.4×10^{-3}, 8.4×10^{-4}, 4.6×10^{-4}, 2.7×10^{-4}, 1.3×10^{-4}, 7.7×10^{-5}, 3.8×10^{-5}, 1.1×10^{-4}, 3.5×10^{-4}, 4.9×10^{-7}, 1.8×10^{-3}, 2.1×10^{-4}, 1.2×10^{-3}, 2.8×10^{-3}, 3.8×10^{-4} and 7.6×10^{-4}. In Fig. 6f, $P = 8.2 \times 10^{-87}$ for Vim$^-$/GFAP$^+$ and Vim$^+$/GFAP$^+$, 2.2×10^{-55} for Vim$^-$/GFAP$^+$ and Vim$^+$/GFAP$^-$ and 1.6×10^{-24} for Vim$^+$/GFAP$^+$ and Vim$^+$/GFAP$^-$. Other exact *P* values are in the figure legends. In Figs. 5b,e and 6f, *P* values were calculated from multiple comparisons tests with one-way ANOVA followed by Holm–Bonferroni's post hoc test on comparing the mean of each column with the mean of every other column. In box plots (Fig. 5j), the center indicates the median, the bottom and top edges of the box indicate the 25th and 75th percentiles, respectively, and the whiskers extend to the minimum and maximum data points. All values of *n* are provided in the figure legends. Statistical source data for Figs. 3, 5 and 6 are provided in the Source Data. Experiments in Fig. 2c,d,e,g and Extended Data Figs. 1–5 were repeated three to five times independently with similar results. Experiments in Figs. 4a,c and 5f and Extended Data Fig. 8 were repeated three times technically on two tissue blocks with similar results.

Reporting Summary. Further information on research design is available in the Nature Research Reporting Summary linked to this article.

Data availability

All data that support the findings of this study are available from the corresponding author upon reasonable request. Source data are provided with this paper.

Code availability

The code used to analyze the data is available from the corresponding author upon reasonable request.

References

59. Biot, E. et al. A new filter for spot extraction in n-dimensional biological imaging. In *2008 5th IEEE International Symposium on Biomedical Imaging: From Nano to Macro* 975–978 (IEEE, 2008).
60. Tun, K. *Graph package* (MATLAB Central File Exchange, accessed 5 May 2021); https://www.mathworks.com/matlabcentral/fileexchange/12648-graph-package

Acknowledgements

We thank R. Yuste, R. Tomer, L. Wei, F. Hu and C. Chen for helpful discussions. W.M. acknowledges support from NIH R01 (GM128214), R01 (GM132860), R01 (EB029523) and US Army (W911NF-19-1-0214).

Author contributions

Lixue Shi and M.W. developed the protocols, performed the experiments and analyzed the data. Y.M. performed MARS probe synthesis and characterization with the help of N.Q. Lingyan Shi contributed to mouse sample preparation. R.A.S. and R.K.P.B. contributed to pancreas sample preparation. Lixue Shi, M.W. and W.M. conceived the concept and wrote the manuscript with input from all authors.

Competing interests

The authors declare no competing interests.

Additional information

Extended data is available for this paper at https://doi.org/10.1038/s41587-021-01041-z.

Supplementary information The online version contains supplementary material available at https://doi.org/10.1038/s41587-021-01041-z.

Correspondence and requests for materials should be addressed to Wei Min.

Peer review information *Nature Biotechnology* thanks Sinem Saka and the other, anonymous, reviewer(s) for their contribution to the peer review of this work.

Reprints and permissions information is available at www.nature.com/reprints.

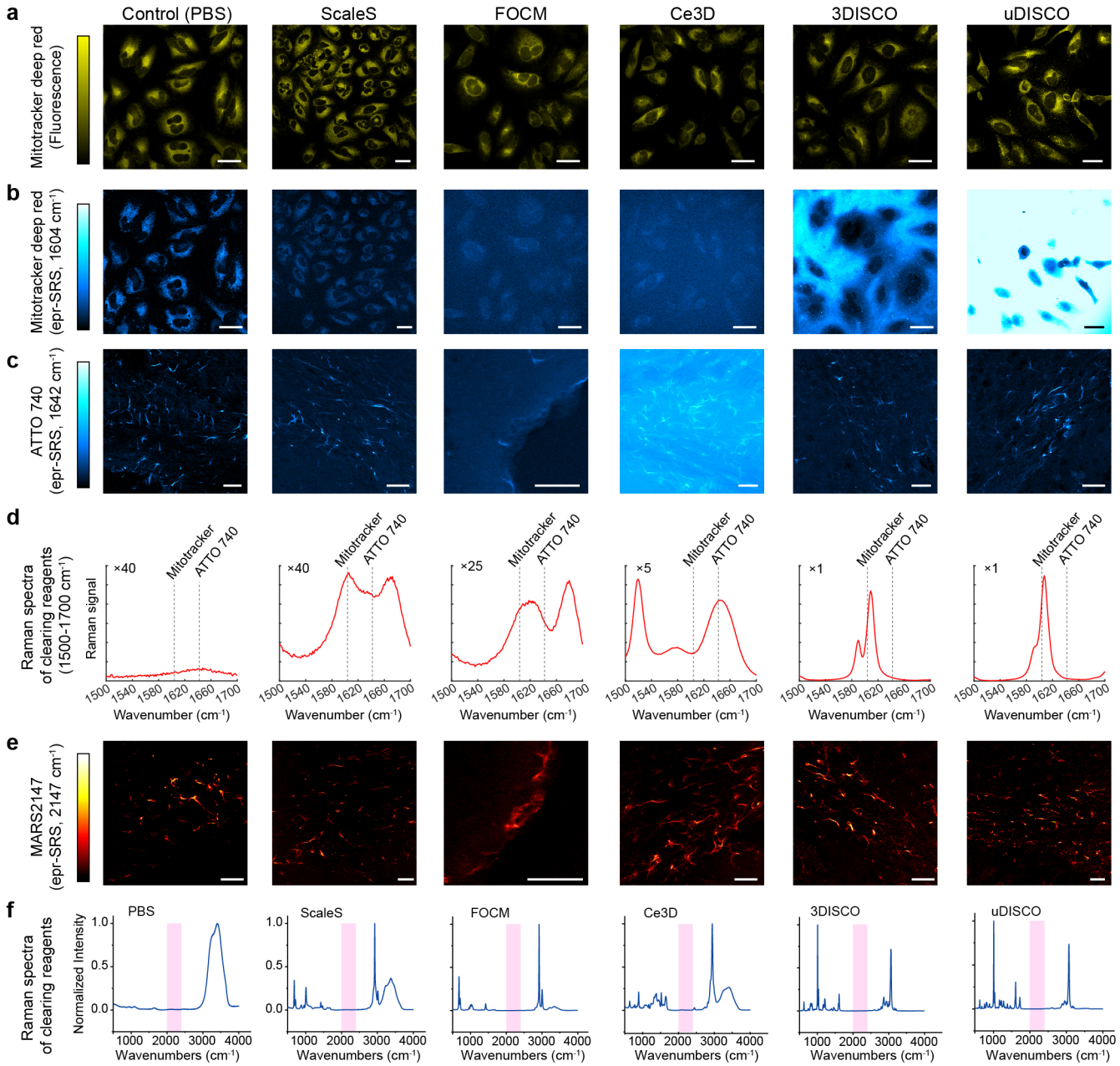

Extended Data Fig. 1 | Testing spectral compatibility between Raman-active dyes and tissue clearing methods. a, **b**, Fluorescence (**a**) and epr-SRS imaging at 1604 cm^{-1} (**b**) of Mitotracker deep red FM (Invitrogen M22426)-stained fixed HeLa cells imaged in different RIMS. **c**, epr-SRS imaging at 1642 cm^{-1} of ATTO 740 stained GFAP on PFA-fixed mouse brain tissue inside different RIMS. **d**, Raman spectra of PBS and RIMS only at 1500–1700 cm^{-1} (spectral window for vibrational peaks of most commercial dyes). Some spectra were amplified by certain folds (number inside) to plot them under a same scale. **e**, epr-SRS imaging at 2147 cm^{-1} of MARS2147 stained GFAP on PFA-fixed mouse brain tissue inside different RIMS. **f**, Full Raman spectra of tissue clearing reagents. The pink area indicates the interested spectral window (2000–2400 cm^{-1}), in which the nitrile-bond reporters in MARS probes vibrate. Spectra in (**d**) and (**f**) were measured with spontaneous Raman spectroscopy. Scale bars, 40 μm.

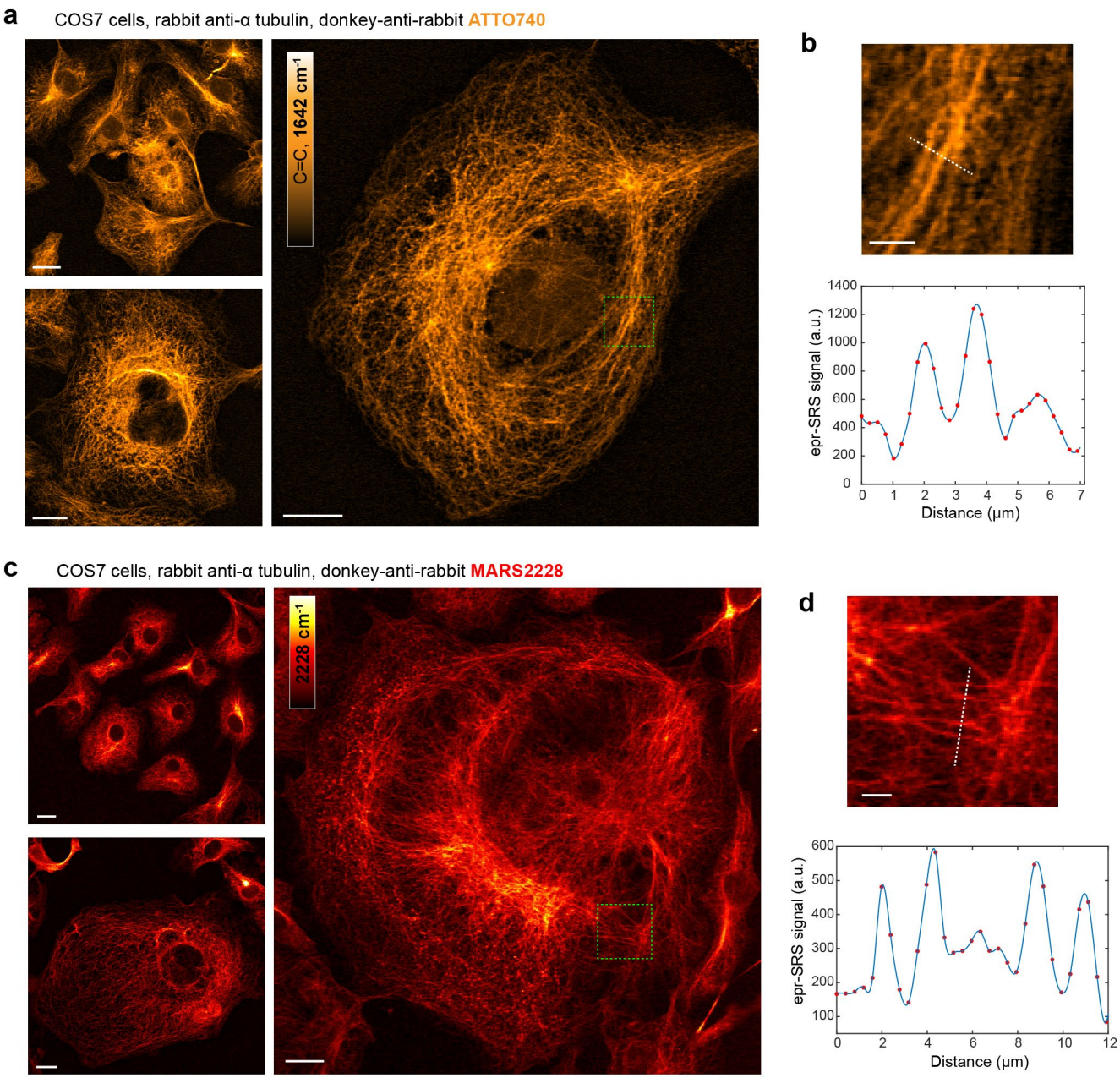

Extended Data Fig. 2 | Demonstration of fine resolution of immuno-eprSRS imaging. α-tubulin in COS7 cells were stained with commercial dye ATTO 740 (**a**-**b**) and MARS2228 (**c**-**d**). **b**, **d**, Magnified regions outlined by the green box in (**a**, **c**), respectively. Below, epr-SRS signal along the white dotted line cut in the magnified images; curves were drawn with a spline fit. Scale bars, 20 μm in (**a**, **c**); 5 μm in (**b**, **d**).

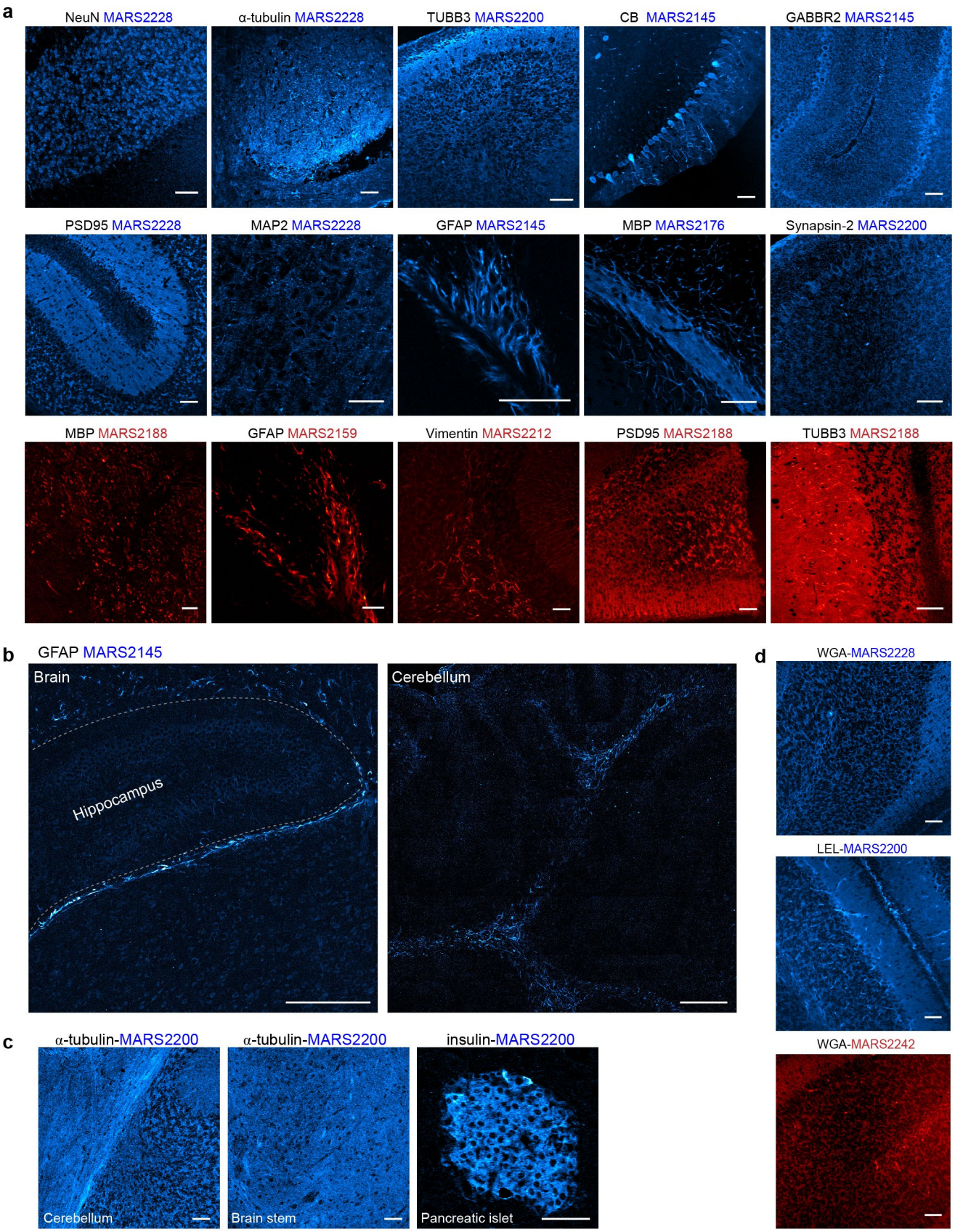

Extended Data Fig. 3 | See next page for caption.

Extended Data Fig. 3 | Immuno-eprSRS imaging with MARS probes in tissue samples. a, Multiple protein targets are compatible with immuno-eprSRS with C-cored MARS probes (in blue) and O-cored MARS probes (in red). Targeted proteins were stained on PFA-fixed mouse brain or cerebellum sections (40-μm thick) with indirect immunostaining. **b**, Mosaic imaging with motorized sample stage. NeuN, neuronal nuclei; TUBB3, β-III-tubulin; CB, calbindin; GABBR2, GABA B receptor 2; PSD95, postsynaptic density protein 95; MAP2, microtubule associated protein 2; GFAP, glial fibrillary acidic protein; MBP, myelin basic protein. **c**, Direct immunostaining with MARS-probe conjugated primary antibodies. **d**, MARS probe-conjugated lectin staining on PFA-fixed cerebellum tissue sections. WGA, wheat germ agglutinin; LEL, *Lycopersicon Esculentum* lectin. More antibody information is in Supplementary Table 3. Scale bars, 50 μm in (**a**) and (**c-d**); 200 μm in (**b**).

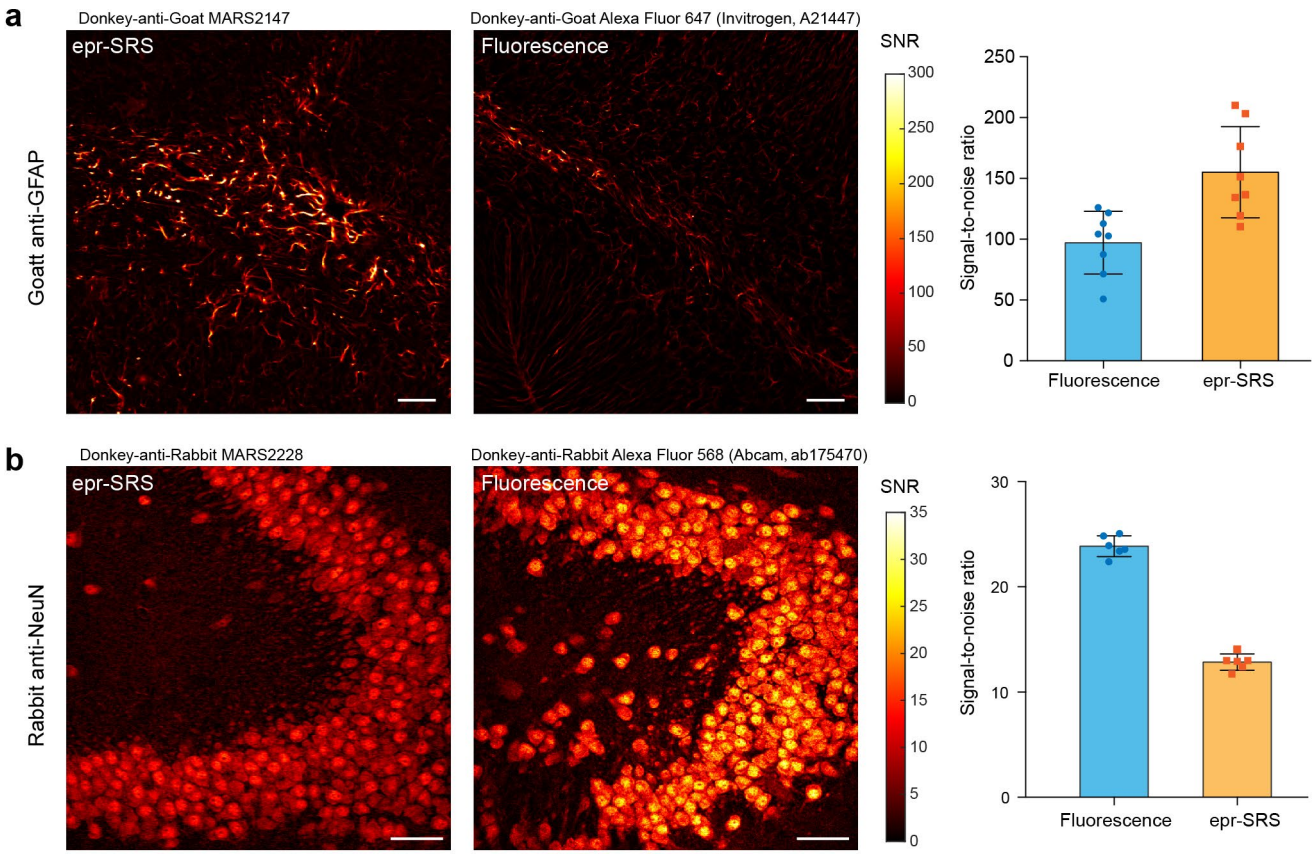

Extended Data Fig. 4 | Quantitative comparison of the signal-to-noise ratios of immuno-eprSRS with standard immunofluorescence. a, Immunostained GFAP in 40-μm thick mouse brain tissue. **b**, Immunostained NeuN in 40-μm thick mouse brain tissue. Each data point of the signal was calculated as the averaged fluorescence/epr-SRS signal of individual nucleus for NeuN or individual astrocytes for GFAP; the noise was measured as the s.d. from tissue areas without stained structures. Pixel dwell time is 2 μs for fluorescence and 80 μs for epr-SRS. Scale bars, 50 μm.

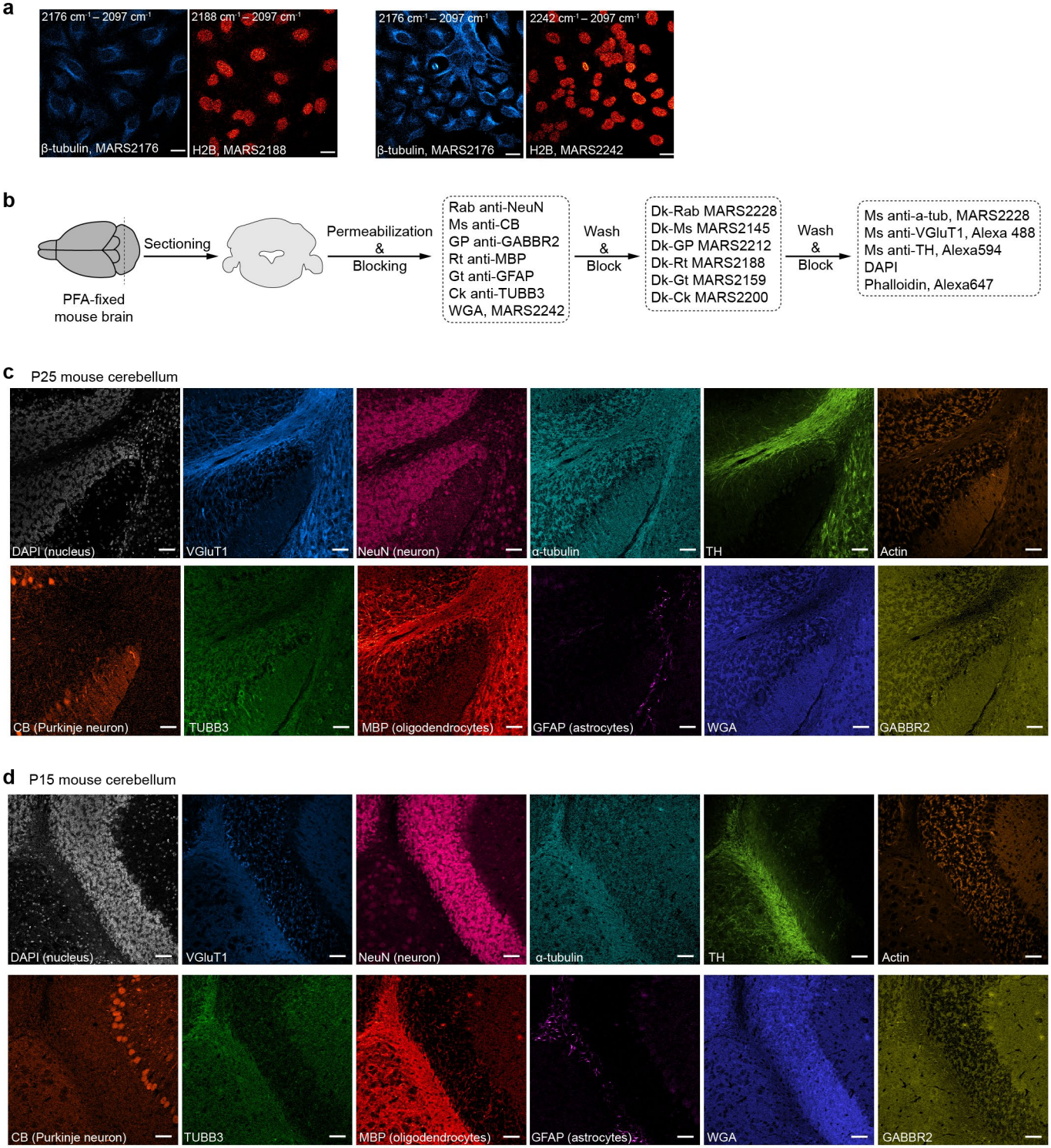

Extended Data Fig. 5 | Simultaneous twelve-target imaging in mouse cerebellum thin sections. a, Two-color imaging tests on fixed cells (nucleus protein H2B labeled by O-cored MARS and cytoskeleton protein β-tubulin labeled by C-cored dyes). No obvious cross-talk between two channels was observed. (left) β-tubulin (labeled by MARS2176) and H2B (labeled by MARS2188). (right) β-tubulin (labeled by MARS2176) and H2B (labeled by MARS2242). **b**, A workflow of multiplexed labeling (also see methods). **c**, **d**, Simultaneous twelve-target protein imaging on cerebellum tissue sections from (**c**) postnatal 25 days (P25) and (**d**) postnatal 15 days (P15) mice. Fluorescence: DAPI (total DNA), vesicular glutamate transporter 1 (VGluT1-Alexa Fluor 488, Glutamatergic neurons, direct immunolabeling), tyrosine hydroxylase (TH-Alexa Fluor 594, Dopaminergic neurons, direct immunolabeling), actin (Phalloidin-Alexa Fluor 647); epr-SRS: neuronal nuclei (NeuN, neurons, MARS2228), α-tubulin-MARS2176 (direct immunolabeling), calbindin (CB, Purkinje neurons, MARS2145), β-III-tubulin (TUBB3, neurons, MARS2200), wheat germ agglutinin (WGA-MARS2242), GABA B receptor 2 (GABBR2, GABAergic neurons, MARS2212), myelin basic protein (MBP; oligodendrocytes, MARS2188), glial fibrillary acidic protein (GFAP, astrocytes and neural stem cells, MARS2159). Scale bars, 20 μm in (**a**); 50 μm in (**c**-**d**).

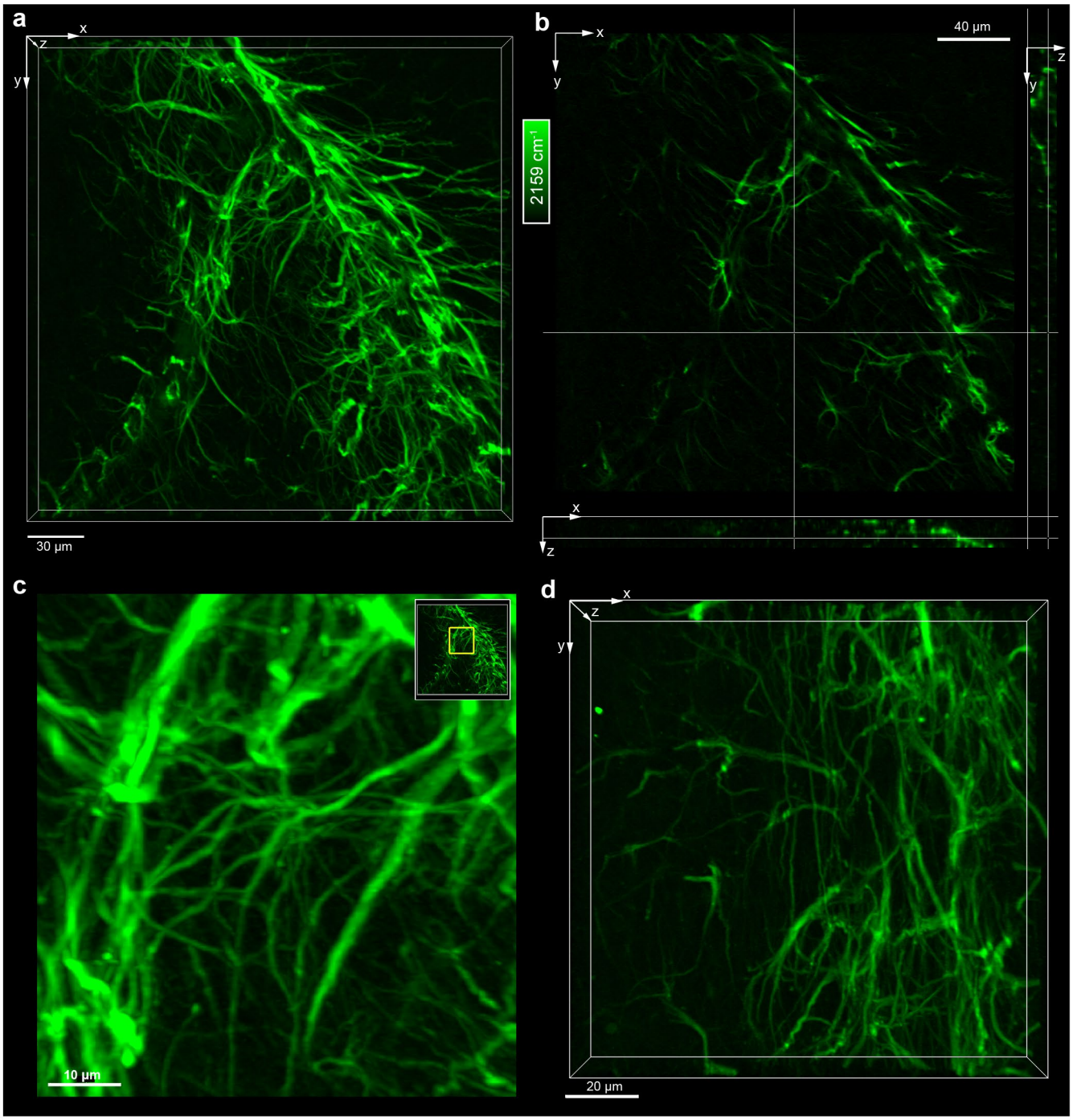

Extended Data Fig. 6 | Sectioning capability and axial resolution of immuno-eprSRS imaging. a, Volume-rendered image; **b**, Orthogonal views; **c**, Zoomed-in volume-rendered image of (**a**); **d**, Optically zoomed-in volume-rendered image of MARS2159 stained GFAP in 100-μm thick mouse brain tissue. The inset yellow box in (**c**) represents the position of the enlarged region. Step size of z is 2 µm in (**a**-**c**) and is 1 µm in (**d**). Scale bars, 30 µm in (**a**); 40 µm in (**b**); 10 µm in (**c**); 20 µm in (**d**).

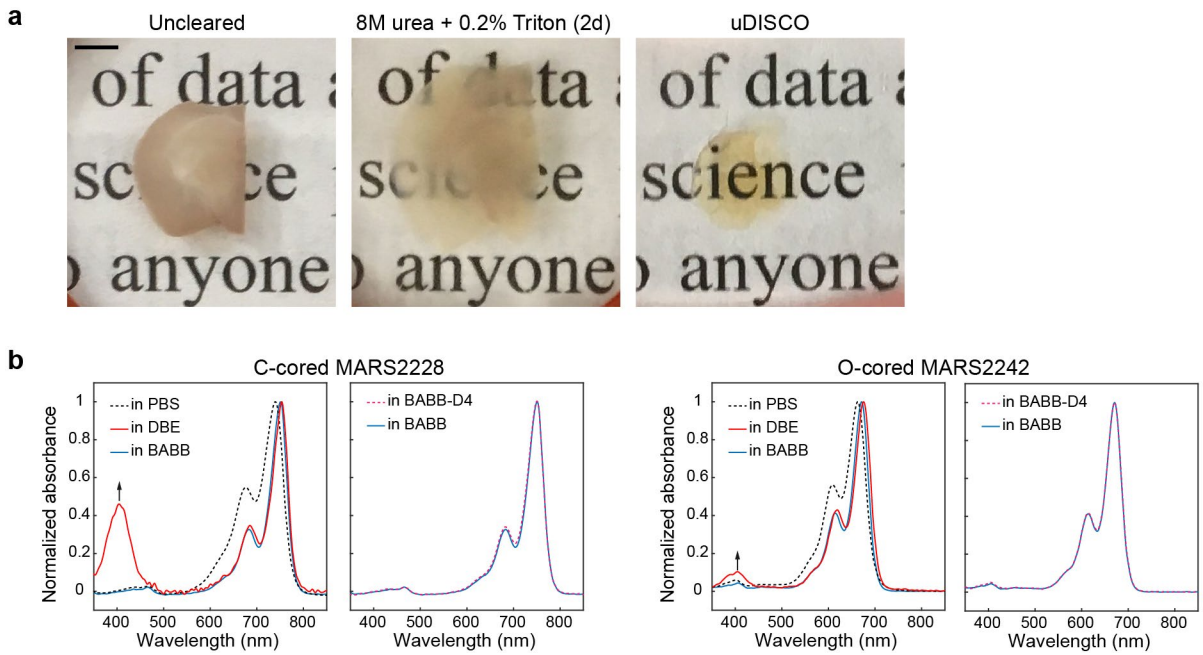

Extended Data Fig. 7 | Tests on immuno-eprSRS for volumetric imaging. a, Photos of 1-mm thick brain slices without clearing (uncleared), cleared by 8 M urea and 0.2% Triton for 2 days and cleared by uDISCO. Scale bar, 2 mm. **b**, Normalized absorption spectra of MARS probes in RI matching solutions in BABB, 3DISCO (DBE) and uDISCO (BABB-D4). A bluer absorption peak appears in DBE, but not in BABB and BABB-D4.

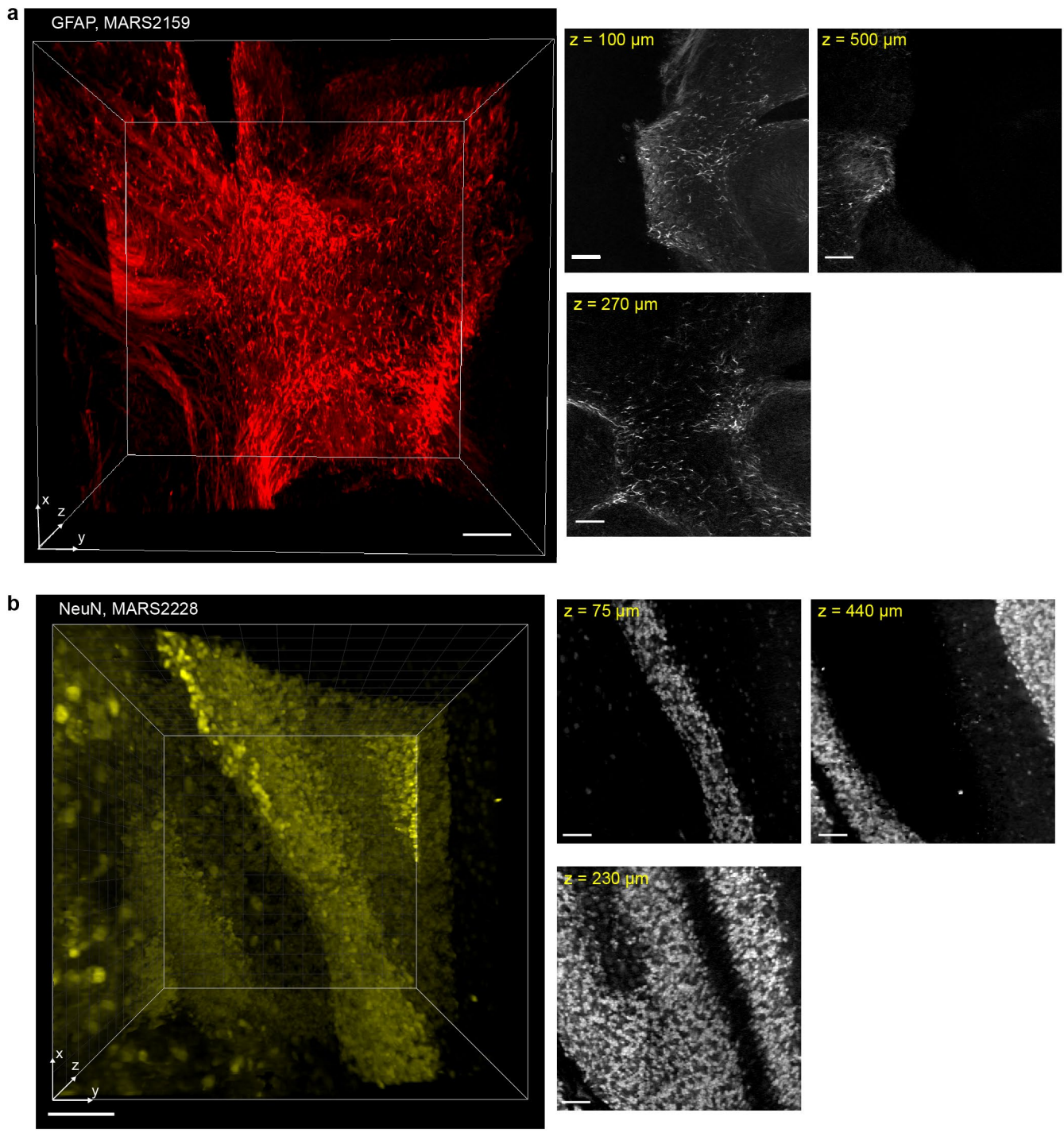

Extended Data Fig. 8 | Volumetric immuno-eprSRS imaging on 500-µm-thick mouse cerebellum sections with uDISCO clearing. a, Volume-rendered image of GFAP (astrocytes) labeled with O-cored MARS2159 in 500-µm thick cerebellum sections cleared by uDISCO. **b**, Volume-rendered image of NeuN (neuronal nucleus) labeled with C-cored MARS2228 in 500-µm thick cerebellum sections cleared by uDISCO. Enlarged images of Fig. 4a. Single-plane images show good epr-SRS contrast along the whole depth for both samples. Scale bars, 100 µm.

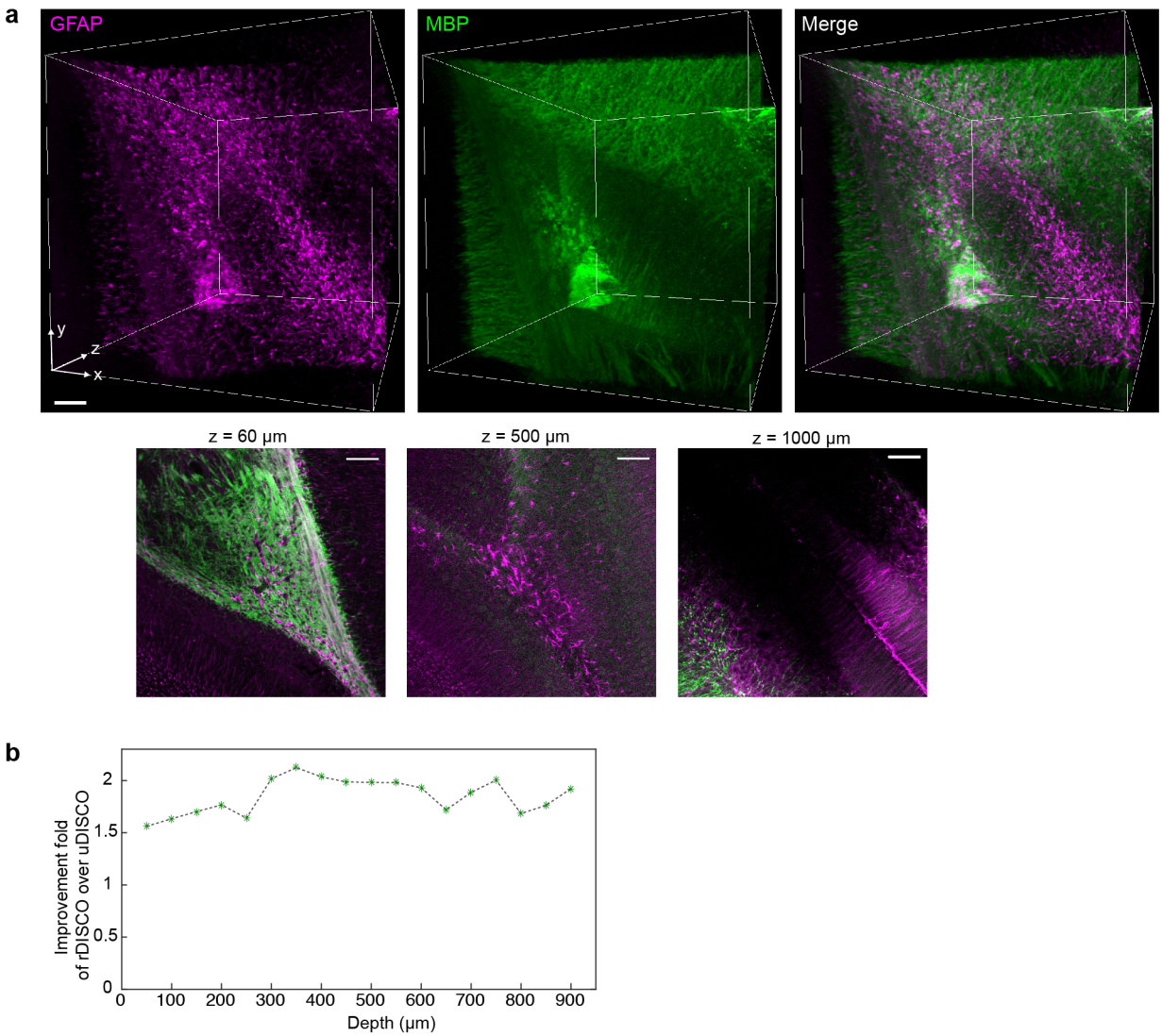

Extended Data Fig. 9 | Improvement of rDISCO over uDISCO on volumetric immuno-eprSRS imaging. a, Volume-rendered images of GFAP (astrocytes, labeled with MARS2228) and MBP (oligodendrocytes, labeled with Alexa Fluor 488) in 1-mm thick cerebellum sections cleared by uDISCO. Two-color merged single-plane images also show good epr-SRS and fluorescence contrast along the whole depth. Scale bars, 100 µm. **b**, SRS signal-to-noise ratio improvement of rDISCO over uDISCO at different depths.

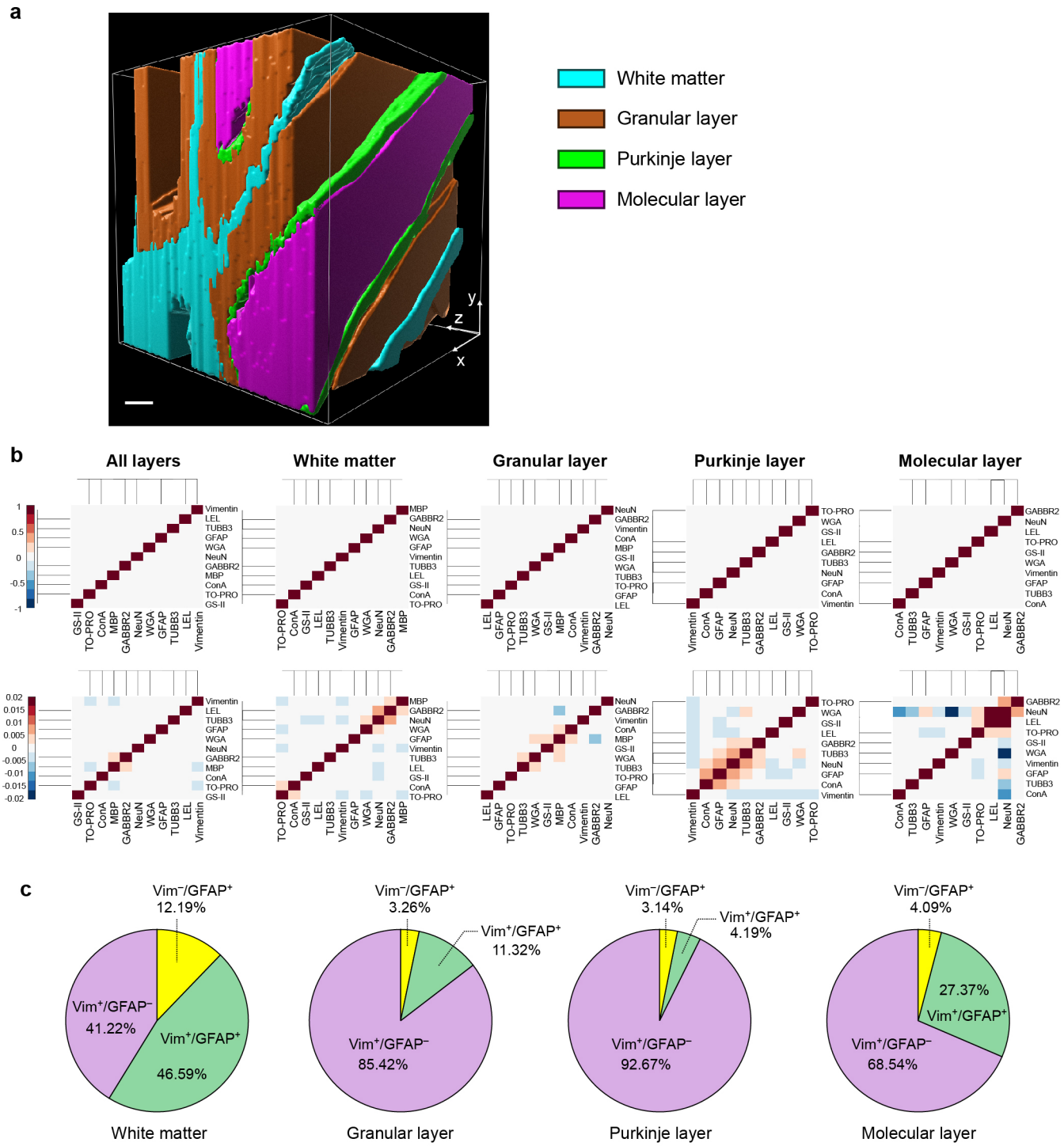

Extended Data Fig. 10 | Quantitative 3D analyses on multiplexed volumetric images. a, Segmentation of four anatomical layers as white matter, the granular layer, the Purkinje layer and the molecular layer. Scale bar, 100 μm. **b**, Correlation heatmaps between randomized images. (up) Color bar plotted in the range of [−1 1]. (down) Color bar plotted in the range of [−0.02 0.02]. **c**, Compositional percentages of $Vim^+/GFAP^-$, $Vim^-/GFAP^+$ and $Vim^+/GFAP^+$ cells for four layers.

nature research

Corresponding author(s): Wei Min

Last updated by author(s): Jul 22, 2021

Reporting Summary

Nature Research wishes to improve the reproducibility of the work that we publish. This form provides structure for consistency and transparency in reporting. For further information on Nature Research policies, see our Editorial Policies and the Editorial Policy Checklist.

Statistics

For all statistical analyses, confirm that the following items are present in the figure legend, table legend, main text, or Methods section.

n/a	Confirmed
☐	☒ The exact sample size (*n*) for each experimental group/condition, given as a discrete number and unit of measurement
☐	☒ A statement on whether measurements were taken from distinct samples or whether the same sample was measured repeatedly
☐	☒ The statistical test(s) used AND whether they are one- or two-sided *Only common tests should be described solely by name; describe more complex techniques in the Methods section.*
☒	☐ A description of all covariates tested
☐	☒ A description of any assumptions or corrections, such as tests of normality and adjustment for multiple comparisons
☐	☒ A full description of the statistical parameters including central tendency (e.g. means) or other basic estimates (e.g. regression coefficient) AND variation (e.g. standard deviation) or associated estimates of uncertainty (e.g. confidence intervals)
☐	☒ For null hypothesis testing, the test statistic (e.g. *F*, *t*, *r*) with confidence intervals, effect sizes, degrees of freedom and *P* value noted *Give P values as exact values whenever suitable.*
☒	☐ For Bayesian analysis, information on the choice of priors and Markov chain Monte Carlo settings
☒	☐ For hierarchical and complex designs, identification of the appropriate level for tests and full reporting of outcomes
☐	☒ Estimates of effect sizes (e.g. Cohen's *d*, Pearson's *r*), indicating how they were calculated

Our web collection on statistics for biologists contains articles on many of the points above.

Software and code

Policy information about availability of computer code

Data collection	SRS data were collected with Olympus FluoView software. Spontaneous Raman spectra were collected with LabSpec6.
Data analysis	Image J 1.52b and custom MATLAB (R2016a) codes were used for image analysis. GraphPad Prism 7 and Origin Pro 8 were used for statistical analysis. Bitplane Imaris was used for 3D rendering, segmentation and distance measurements.

For manuscripts utilizing custom algorithms or software that are central to the research but not yet described in published literature, software must be made available to editors and reviewers. We strongly encourage code deposition in a community repository (e.g. GitHub). See the Nature Research guidelines for submitting code & software for further information.

Data

Policy information about availability of data

All manuscripts must include a data availability statement. This statement should provide the following information, where applicable:

- Accession codes, unique identifiers, or web links for publicly available datasets
- A list of figures that have associated raw data
- A description of any restrictions on data availability

The authors declare that all data supporting the results in this study are available within the paper and its Supplementary Information. All raw and processed images generated in this work are available from the corresponding author on reasonable request.

Field-specific reporting

Please select the one below that is the best fit for your research. If you are not sure, read the appropriate sections before making your selection.

☒ Life sciences ☐ Behavioural & social sciences ☐ Ecological, evolutionary & environmental sciences

For a reference copy of the document with all sections, see nature.com/documents/nr-reporting-summary-flat.pdf

Life sciences study design

All studies must disclose on these points even when the disclosure is negative.

Sample size	ROIs from different parts of the tissue section were used for quantification of signal-to-noise ratios. Number of ROIs were noted in the figure legends. For relative thin samples (not thicker than 100 um), n=6-12 ROIs were used. For thick sections (>500-um thickness), n=3 ROIs were used.
Data exclusions	No data were excluded.
Replication	At least three replicates were performed with independent measurement and analysis. The results were reproducible.
Randomization	Randomization was not necessary for this study.
Blinding	Blinding was not pertinent to this study as experimental conditions were mostly evident from the image data.

Reporting for specific materials, systems and methods

We require information from authors about some types of materials, experimental systems and methods used in many studies. Here, indicate whether each material, system or method listed is relevant to your study. If you are not sure if a list item applies to your research, read the appropriate section before selecting a response.

Materials & experimental systems

n/a	Involved in the study
☐	☒ Antibodies
☐	☒ Eukaryotic cell lines
☒	☐ Palaeontology and archaeology
☐	☒ Animals and other organisms
☒	☐ Human research participants
☒	☐ Clinical data
☒	☐ Dual use research of concern

Methods

n/a	Involved in the study
☒	☐ ChIP-seq
☒	☐ Flow cytometry
☒	☐ MRI-based neuroimaging

Antibodies

Antibodies used

The full list of antibodies is also available in Supplementary information

rabbit anti-a-tubulin (Abcam, Cat# ab18251, polyclonal, diluted 1:100)
rabbit anti-a-tubulin (Abcam, Cat# ab52866, clone: EP1332Y, diluted 1:100)
mouse anti-a-tubulin (BioLegend, Cat# 625902, clone: TU-01, diluted 1:40 after MARS probe conjugation)
mouse anti-b-III-tubulin (BioLegend, Cat#657402, clone: AA10, diluted 1:100)
chicken anti-b-III-tubulin (Abcam, Cat# ab41489, polyclonal, diluted 1:100-1:50)
mouse anti-b-tubulin (Abcam, Cat# ab131205, diluted 1:100)
mouse anti-calbindin (Abcam, Cat# ab82812, clone: CB-955, diluted 1:100-1:40)
mouse anti-cytokeratin 18 (Abcam, Cat# ab7797, clone: DC-10, diluted 1:100)
rabbit anti-cytokeratin 18 (Abcam, Cat# ab24561, polyclonal, diluted 1:100)
rabbit anti-EpCAM (Abcam, Cat# ab71916, polyclonal, diluted 1:100)
rabbit anti-fibrillarin (Abcam, Cat# ab5821, polyclonal, diluted 1:100)
rabbit anti-Giantin (Abcam, Cat# ab24586, polyclonal, diluted 1:100)
rabbit anti-H2B (Abcam, Cat# ab1790, polyclonal, diluted 1:100)
rabbit anti-MAP2 (BioLegend, Cat# 801810, clone: SMI 52, diluted 1:100)
mouse anti-vimentin (Abcam, Cat# ab8069, clone: V9, diluted 1:50)
mouse anti-Glucagon (Santa Cruz Biotechnology, Cat# sc-514592, clone: C-11, diluted 1:50)
rabbit anti-insulin (Invitrogen, Cat# 701265, clone: 19H4L12, diluted 1:50 after MARS probe conjugation)
rabbit anti-PSD95 (Invitrogen, Cat# 51-6900, polyclonal, diluted 1:50)
sheep anti-synapsin 2 (ThermoFisher, Cat# OSS00073G, polyclonal, diluted 1:100)
rat anti-MBP (Abcam, Cat# ab7349, clone: 12, diluted 1:100-1:20)
rabbit anti-NeuN (Invitrogen, Cat# PA5-78639, polyclonal, diluted 1:100-1:20)

guinea pig anti-GABBR2 (Millipore Sigma, Cat# AB2255, polyclonal, diluted 1:100-1:40)
goat anti-GFAP (ThermoFisher, Cat# PA5-18598, polyclonal, diluted 1:100-1:20)
chicken anti-vimentin (Abcam, Cat# ab41489, polyclonal, diluted 1:100-1:20)
mouse anti-VGluT1, Alexa Fluor 488 (Abcam, Cat# ab193595, clone: N28-9, diluted 1:50)
mouse anti-TH, Alexa Fluor 594 (BioLegend, Cat# 818003,clone: 2/40/15, diluted 1:50)
mouse anti-b-III-tubulin, Alexa Fluor 594 (BioLegend, Cat# 657408, clone: AA10, diluted 1:40)

Secondary antibodies for MARS probe conjugation (All from Jackson ImmunoResearch)
Donkey anti-Guinea pig IgG (H+L), Cat# 706-005-148, diluted 1:200-1:40 after conjugation
Donkey anti-Goat IgG (H+L), Cat# 705-005-147, diluted 1:200-1:40 after conjugation
Donkey anti-Chicken IgY (H+L), Cat# 703-005-155, diluted 1:200-1:40 after conjugation
Donkey anti-Rabbit IgG (H+L), Cat# 711-005-152, diluted 1:200-1:40after conjugation
Donkey anti-Rat IgG (H+L), Cat# 712-005-153, diluted 1:200-1:40 after conjugation
Donkey anti-Mouse IgG (H+L), Cat# 715-005-151, diluted 1:200-1:40 after conjugation
Donkey anti-Sheep IgG (H+L), Cat# 713-005-147, diluted 1:200-1:40 after conjugation

Fluorophore-conjugated secondary antibodies used for reference imaging:
Donkey anti-Rabbit-Alexa568 IgG (H+L) (Invitrogen, Cat# A10042, diluted 1:500-1:200)
Donkey anti-Rat-Alexa488 IgG (H+L) (Abcam, Cat# ab150153, diluted 1:500-1:200)
Donkey anti-Chicken-Cy3 IgY (H+L) (Jackson ImmunoResearch, Cat# 703-165-155, diluted 1:500-1:200)
Donkey anti-Guinea pig-Cy5 IgG(H+L) (Jackson ImmunoResearch, Cat# 706-175-148, diluted 1:500-1:200)
Donkey anti-Mouse-Alexa594 IgG (H+L) (Invitrogen, Cat# A21203, diluted 1:500-1:200)
Donkey anti-Goat-Alexa647 IgG (H+L) (Invitrogen, Cat# A21447, diluted 1:500-1:200)

Validation

All antibodies used are from commercial sources as described and were validated by the manufacturer. The validation and references for each antibody are available on the respective vendor websites that can reached via the catalog numbers listed above. Most of the antibodies have been tested suitable for IHC/IF based on vendor websites or several references. In our experiments, epr-SRS imaging patterns are consistent with reference IF patterns and matched the distribution that these antibodies were expected to label based on the literature, for both direct and indirect immunolabeling.

Eukaryotic cell lines

Policy information about cell lines

Cell line source(s)	Cell lines were purchased from ATCC including HeLa (ATCC CCL-2), COS-7 (ATCC CRL-1651) and MCF7 (ATCC HTB-22).
Authentication	ATCC authenticated the cells.
Mycoplasma contamination	Cell lines were not tested for mycoplasma contamination.
Commonly misidentified lines (See ICLAC register)	No commonly misidentified cell lines were used.

Animals and other organisms

Policy information about studies involving animals; ARRIVE guidelines recommended for reporting animal research

Laboratory animals	Wild type male and female mice of strain C57BL/6 (15-25 days old and 8-12 weeks old) were used in this study.
Wild animals	The study did not involve wild animals.
Field-collected samples	The study did not involve samples collected from the field.
Ethics oversight	All animal experiments were conducted in adherence to the experimental protocol approved by Columbia University IACUC (AC-AABD1552) or IACUC of University of Colorado Anschutz Medical campus (#00024).

Note that full information on the approval of the study protocol must also be provided in the manuscript.